*energies*

MDPI

*Article*

# Robust Dynamic Control of Constant-Current-Source-Based Dual-Active-Bridge DC/DC Converter Used for Off-Board EV Charging

**Muhammad Husnain Ashfaq [1], Zulfiqar Ali Memon [2], Muhammad Akmal Chaudhary [2], Muhammad Talha [1], Jeyraj Selvaraj [1,*], Nasrudin Abd Rahim [1] and Muhammad Majid Hussain [3,*]**

[1] UM Power Energy Dedicated Advanced Centre (UMPEDAC), University of Malaya, Kuala Lumpur 59990, Malaysia
[2] Department of Electrical and Computer Engineering, Ajman University, Ajman P.O. Box 346, United Arab Emirates
[3] Electrical, Electronic & Computer Engineering, School of Engineering & Physical Sciences, Heriot-Watt University, Edinburgh EH14 4AS, UK
* Correspondence: jeyraj@um.edu.my (J.S.); muhammad.hussain@hw.ac.uk (M.M.H.)

**Abstract:** Due to the high power density, inherent zero-voltage-switching (ZVS), and high voltage-conversation ratio, the current source-based isolated dual-active-bridge DAB–DC/DC converters are extensively used for charging EVs under constant-current mode. However, the fast dynamic response of an output current is a crucial requirement for dual-active-bridge DC/DC converters operating as a constant-current source. This study proposes a fast current controller (FCC) for tracking the desired output current under various input/output parameter disturbances/variations. The proposed control strategy can ensure a fast transient response with negligible overshoot/undershoot for output current during start-up and when there are variations in the load or input voltage. Furthermore, the dynamic behavior of the current control against change in the reference current value has also been improved. A constant-current-based DAB–DC/DC converter is modeled and simulated in MATLAB/Simulink software and a scaled-down 300 W lab prototype DAB–DC/DC converter is designed with the TMS320F28335 DSP controller of Texas Instruments. To verify the effectiveness of the proposed current controller, different test cases, such as a change in the load, a change in the input voltage, and a change in the desired output current, are considered. Moreover, under these test cases, the proposed current-control strategy is compared with the conventional proportional–integral (PI) current controller, model-based phase-shift controller (MBPS), and load current feed-forward controller (LCFF). Both the experimental and simulation results have validated the effectiveness of the proposed control strategy.

**Keywords:** renewable energy; bidirectional DAB–DC/DC converter; constant-current control; fast dynamic performance; off-board EV charging

check for updates

**Citation:** Ashfaq, M.H.; Memon, Z.A.; Chaudhary, M.A.; Talha, M.; Selvaraj, J.; Rahim, N.A.; Hussain, M.M. Robust Dynamic Control of Constant-Current-Source-Based Dual-Active-Bridge DC/DC Converter Used for Off-Board EV Charging. *Energies* **2022**, *15*, 8850. https://doi.org/10.3390/en15238850

Academic Editor: Mario Marchesoni

Received: 7 October 2022
Accepted: 19 November 2022
Published: 23 November 2022

**Publisher's Note:** MDPI stays neutral with regard to jurisdictional claims in published maps and institutional affiliations.

**Copyright:** © 2022 by the authors. Licensee MDPI, Basel, Switzerland. This article is an open access article distributed under the terms and conditions of the Creative Commons Attribution (CC BY) license (https://creativecommons.org/licenses/by/4.0/).

## 1. Introduction

The combustion of fossil fuels in the transport, private, and industrial sectors is contributing massively to greenhouse gases and becoming a vital issue for the world environment. Climate change, rising energy costs, and the interminable exhaustion of fossil fuels are the vital challenges of the present world. All these challenges are directly associated with above-stated three main sectors, which are heavily utilizing fossil fuels and emitting greenhouse gases into the atmosphere [1–3]. Globally, many countries are striving to reduce the reliance on fossil fuels and replace them with cleaner energy. In contrast to the other two sectors, the transport sector adds 23% of carbon dioxide to the world atmosphere, which is a worrisome threat to climate change [4]. Moreover, with the fast urbanization and rise in population, vehicular emissions are rising continuously at a

rapid pace. However, with the electrification of transport and the penetration of electrical vehicles (EVs), it is possible to reduce the carbon dioxide footprint from the environment [5]. Recently, the rapid growth in the penetration of EVs has been observed. In 2018, global EVs surpassed 5100 thousand, and by the end of 2050, this number is foreseen to cross the 100 million mark [6]. Despite the high penetration of EVs, range anxiety is one of the major hurdles in the fast adaption of EVs. To address this range anxiety issue, researchers have shifted towards off-board DC fast chargers. As shown in the Figure 1, off-board DC fast chargers have two power conversion stages: an AC/DC rectification and an isolated DC/DC converter. In the first stage, the AC/DC rectifier converts grid AC input voltage into an intermediate DC voltage. In the second stage, the DC/DC converter converts the intermediate DC voltage into the desired battery-rated voltage [7]. Much research has already been done on the first stage (AC–DC rectifier), and an efficiency of approximately 98% has been reported [8]. However, for the second stage (DC–DC converter), there is room for more advanced research. Therefore, from now on, the first stage will not be discussed; rather, only the second stage will be discussed in this paper.

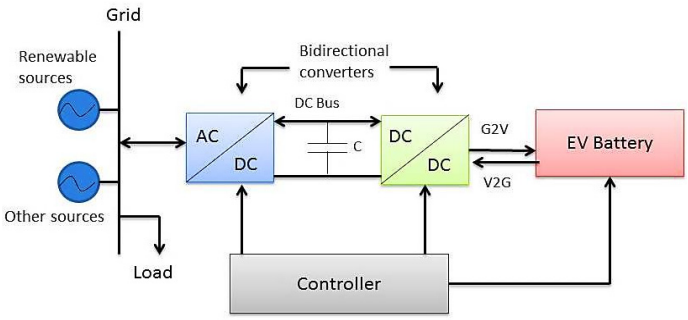


**Figure 1.** Two-stage off-board DC charger for EVS.

The dual-active-bridge (DAB–DC/DC) converter as shown in the Figure 2 was first reported in the early 1990s [9,10]. Due to its various features such as the high power density, inherent zero-voltage-switching (ZVS), high voltage-conversation ratio, galvanic isolation, and symmetric structure [11,12], it is the most preferred choice and is widely used at the second stage of an off-board EV charger [13]. Constant current (CC) is the most common method used for charging the EV's battery. Under CC mode, the DAB–DC/DC converter operates as a regulated current source [14]. The DAB–DC/DC converter may encounter some severe situations, such as: fluctuation in the input supply voltage, load disturbances, etc. Therefore, a fast and robust dynamic response of the output current control is a vital requirement for the DAB–DC/DC converter to tackle these extreme conditions [15]. To enhance the dynamic performance, various control methods have been reported in the literature. These control methods are classified as follows:

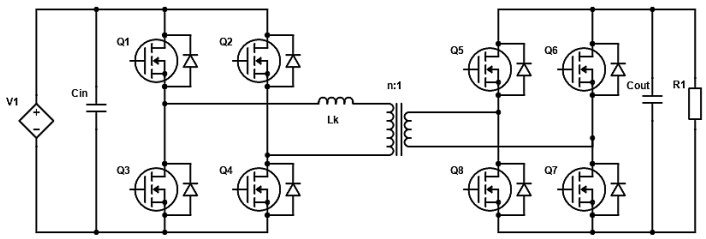


**Figure 2.** DAB–DC/DC converter topology.

A traditional method of controlling the DAB–DC/DC converter output current is proportional–integral (PI)-controller-based closed-loop current-feedback control [16,17]. The difference between the desired current and the output current of the converter is fed to the PI controller as an input. In order to track the desired current, the phase-shift ratio between two bridges is adjusted by the output of the PI controller. This approach has a

simple design structure and requires less sampling [18]. However, the major drawback of this method is that it cannot attain optimum control over the entire power range because the PI controller is a linear system and has a fixed controller gain. However, the DAB–DC/DC is a nonlinear system, and its gain depends on the loading condition. A larger controller gain is required under heavy loads, whereas a smaller controller gain is required under light loads. Thus, to achieve excellent dynamic performance, the controller gain needs to be adjusted according to the loading condition during each cycle of control. To address this issue, a lookup-table-based solution is proposed in [19]. The gain of the controller is adjusted according to the loading power. However, this method lacks accuracy, as it is not very easy to tune the controller gain accurately during the runtime.

The load current disruptions caused by load variations are also an important element that influences the dynamic performance of the output current and are not examined in the abovementioned control methods. G. Holmes et al. has proposed the load current feed-forward control method to tackle these load current disruptions. The dual-loop control with an inner current and outer voltage loop is used to enhance the current and voltage recovery performance during load changes [20]. However, the feed-forward coefficient of the load current changes with the loading power. Thus, this limits its application in DAB–DC/DC converters. Similar to [19], a lookup-table-based approach is used in [21]. The feed-forward coefficient is adjusted according to the loading power. However, again this approach lacks accuracy, and the lookup tables occupied a large amount of memory of the DSP controller.

Based on the LCFF control method, a model-based phase-shift control (MBPS) is reported in [22]. In this proposed control method, the feed-forward coefficient is adjusted during the runtime by calculating the load power. However, the MBPS control proposed in this study is employed to compensate for the current and voltage feedback of the PI controller and the dynamic performance of the converter still depends on the load power. Thus, this control method also needs a small gain during light loading conditions and a large gain during heavy loading conditions.

Recently, intelligent nonlinear controllers have become popular among researchers, and they are very effective when the process complexity is high, including uncertainty and nonlinear behavior, and the exact mathematical model of the system is not known [23,24]. To enhance the dynamic performance of the DAB–DC/DC converter, various nonlinear control methods, such as model-predictive control, sliding-mode control, and fuzzy-neural control, have been proposed [25–31]. However, although these control methods have enhanced the dynamic performance of the system to some extent, since the exact mathematical model of the DAB–DC/DC converter is known and has been reported in various studies [32,33], implementing these control methods will make the system too complex and tedious to be realized in practice [34]. Direct power control is a compelling approach that has been extensively used for front-end rectifiers and grid-connected inverters [35–38]. In this control strategy, the required output power is tracked to enhance the dynamic performance of the controller. Therefore, this control method would be a better option compared to the other methods mentioned above. This control method has been implemented for voltage-source-based DAB–DC/DC converters and reported in the literature [39,40]. However, according to the authors' fullest knowledge, this control method has not been yet implemented for current-source-based DAB–DC/DC converters.

Contribution: Based on direct-power control principles, a robust dynamic current controller for the current-source-based DAB–DC/DC converter is proposed in this study to track the desired output current under various input/output parameter variations. The proposed control strategy can ensure a fast transient response with negligible overshoot/undershoot for the output current during start-up and when there are variations in the load or input voltage. Furthermore, the dynamic behavior of the current control has also been improved against change in the reference-current value. Unlike other control strategies reported in the literature, the proposed control scheme does not require a lookup table or changes in controller parameters during the runtime. In contrast with the model-based phase-shift controller, the proposed controller design is very simple, as it

does not need some circuit parameters such as inductor value, transformer turns ratio, and switching frequency to calculate the desired phase-shift ratio. An experimental comparison of the conventional PI current controller, model-based phase-shift controller, load current feed-forward controller, and proposed fast current controller is performed to demonstrate the salient features and superior performance of the proposed control strategy.

The organization of the rest of paper is as follows: In Section 2, the workings and characteristics of the DAB–DC/DC converter with a single-phase-shift modulation technique is analyzed. In Section 3, the controller is proposed, and the mathematical model and small-signal analysis is done to analyze the dynamic characteristics of the system. In Sections 4 and 5, the simulation and hardware results of the proposed controller are compared with other control methods and discussed in detail to verify the effectiveness of the theoretical analysis of the proposed controller. Based on the results, the conclusion is drawn in Section 6.

## 2. Working of Single-Phase-Shift DAB–DC/DC Converter

The transmission of power between two H-bridges in the DAB–DC/DC converter is similar to the power flow between two voltage buses in a power system; consider two voltage sources, $V_1$, and $V_2$, connected by a line reactance L, as shown in the Figure 3. As the voltage source $V_1$ is leading the voltage source $V_2$, the power transfer takes place in the forward direction (left to right) and is given as [41]

$$P = \frac{V_1 \times V_2 \times Sin\varphi}{w \times L} \quad (1)$$

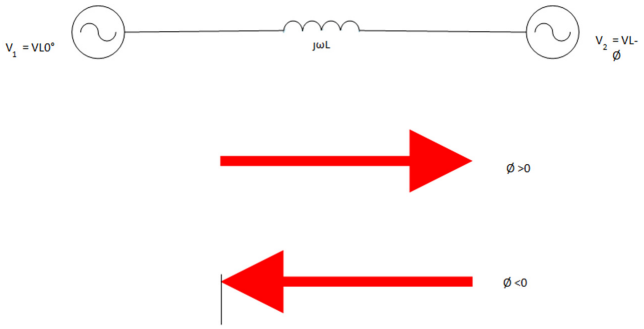


**Figure 3.** Transfer of power between two voltage buses.

Figure 4 shows the equivalent model of the isolated DAB–DC/DC converter. Lk is the total inductance (sum of auxiliary inductance and the transformer's leakage inductance); $V_1$ is the high-frequency square-wave output voltage of bridge-1, and $V_2$ is the high-frequency square-wave input voltage for bridge-2, whereas $V_L$ and $i_L$ indicate the voltage and current of the $L_k$, and N is the turn ratio of the high-frequency isolated transformer. These high-frequency square waves have a phase shift in between them, and the transfer for power takes place from the leading bridge to the lagging bridge. By reversing the phase shift between these two bridges, the bidirectional flow of power can easily be attained. The single-phase-shift (SPS)-modulation technique is the most common and widely used technique for the DAB–DC/DC converter. Simplicity is the main advantage of this modulation technique. In the SPS DAB–DC/DC converter, the primary-side switches and secondary-side switches operate at a constant 50% duty cycle. To generate square-wave output, the cross-connected switches turn on and turn off simultaneously [42]. The switching sequence of the primary and secondary bridge is shown in Figure 5. It can be seen that a phase shift is introduced between these two bridges of the converter. Due to this phase shift, a voltage difference is induced and the current flows from the leading bridge to the lagging bridge. The transmission of power in the SPS DAB–DC/DC converter is expressed as [43]

$$P = NV_1V_2D(1 - D)/2F_sL \quad (2)$$

During different switching sequences, the current flowing through the leakage inductor can divided into four time intervals, and is expressed as:

$$i_{Lk}(t) = \begin{cases} i_{Lk}(0) + 1/L_k\,(V_1 + NV_2)\Delta t & (0 < \mathrm{t} < \mathrm{t1}) \\ i_{Lk}(t_1) + 1/L_k\,(V_1 - NV_2)\Delta t & (\mathrm{t1} < \mathrm{t} < \mathrm{t2}) \\ i_{Lk}(t_2) + 1/L_k\,(-V_1 - NV_2)\Delta t & (\mathrm{t2} < \mathrm{t} < \mathrm{t3}) \\ i_{Lk}(t_3) + 1/L_k\,(-V_1 + NV_2)\Delta t & (\mathrm{t3} < \mathrm{t} < \mathrm{t4}) \end{cases} \quad (3)$$

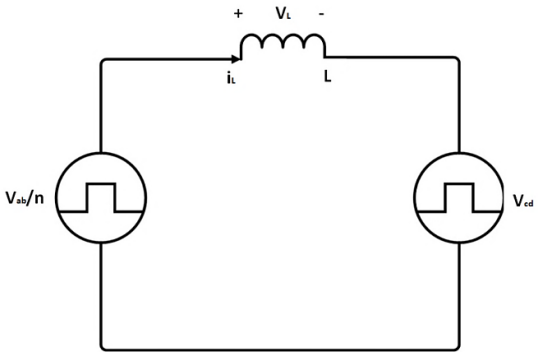


**Figure 4.** Equivalent model of DAB–DC/DC converter.

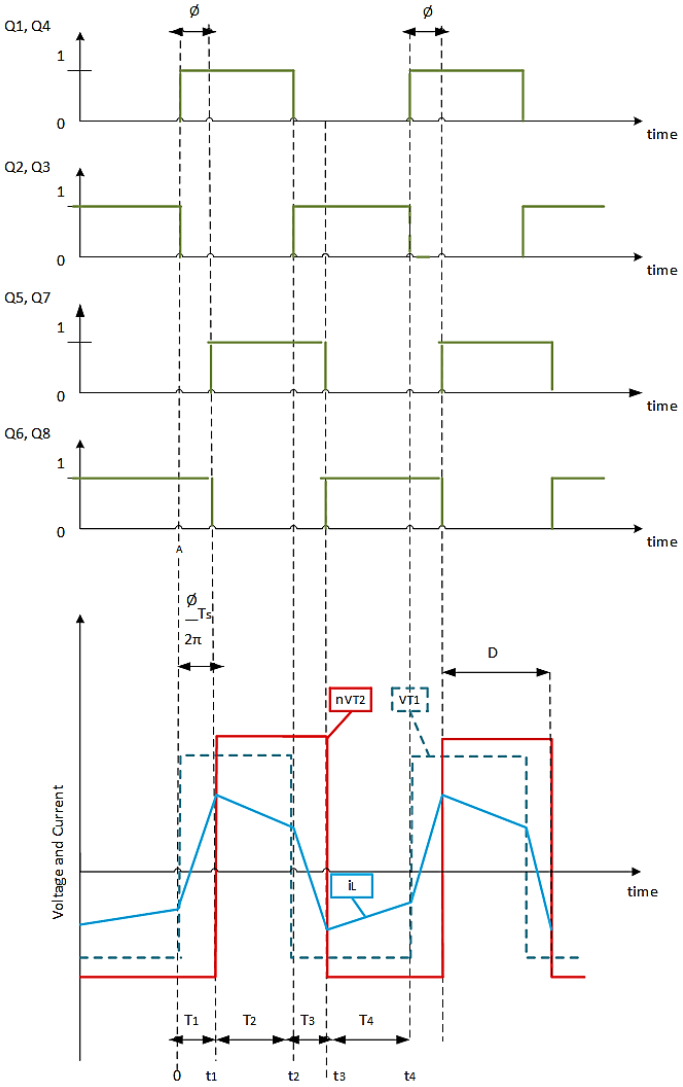


**Figure 5.** Voltage, inductor current, and switching signals for SPS DAB–DC/DC converter.

## 3. Proposed Fast Current Controller (FCC)

A direct power control strategy is one of the efficient techniques to enhance the dynamic response of DAB–DC-DC converters. The main concept of this control strategy is to track the required output power immediately to attain an excellent dynamic response. Therefore, to fulfill the desired power demand, the relation between input and output transmitted power should be defined. In practical applications, the losses in the DAB–DC/DC converter cannot be neglected, and the required output power cannot be obtained by simply multiplying the output voltage with the desired output current. Due to losses in the converter, the input side and output side transmission power cannot be the same. Therefore, based on the direct power control and energy principle, an implicit power-based fast current control (FCC) is proposed to compensate these power losses in the current-source-based DAB–DC/DC converter, as shown in Figure 6.

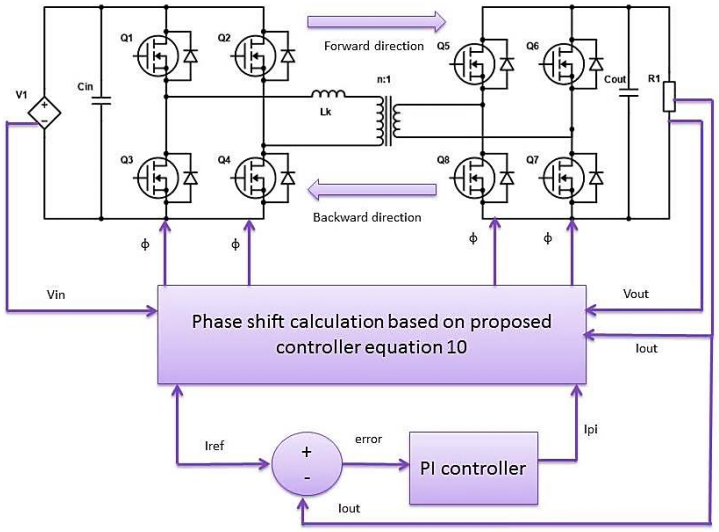


**Figure 6.** Block representation of proposed fast current controller for SPS DAB–DC/DC converter.

The Equation (2) can be written as

$$PF_sL/N = V_{in}V_{out}D(1-D)/2 \tag{4}$$

For a given desired active power $(P_*)$, the term $F_sL/N$ is constant, so we can rewrite Equation (4) as

$$P_* = V_{in}V_{out}D(1-D)/2 \tag{5}$$

Rearranging Equation (5)

$$D = 1/2 - \sqrt{1/4 - 2P_*/V_{in}V_{out}} \tag{6}$$

$$P_* = (V_*I_*) \tag{7}$$

where $I_*$ is the desired current obtained by the output of PI controller and the desired voltage $V_*$ can be expressed as:

$$V_* = I_{o_{ref}}V_{out}/I_{out} \tag{8}$$

$$P_* = \left(I_{o_{ref}}V_{out}/I_{out}\right)(I_*) \tag{9}$$

By putting value of $P_*$ in Equation (6) and then simplifying, the desired phase-shift ratio can be expressed as

$$D = 1/2 - \sqrt{1/4 - 2I_{o_{ref}}I_*/V_{in}I_{out}} \tag{10}$$

The output of the PI current controller should be in the following range

$$|I_*| \in \left[0, V_{in} I_{out} / 8 I_{o_{ref}}\right] \tag{11}$$

From Equation (10), the desired phase-shift ratio $D$ is calculated. Finally, based on this single-phase-shift ratio, switching signals are generated and fed to the DAB–DC/DC converter switches in order to achieve the desired output power.

### *3.1. Mathematical MODEL of DAB–DC/DC Converter*

The concept of the generalized-average-modeling approach for DC/DC converters is discussed in [44]. This is an effective way to analyze power electronics converters [45]. Using the same concept, a generalized-average-modeling method for the triple-phase-shift (TPS)-based DAB–DC/DC converter is proposed by Rolak et al. [46]. In this method, the state-space equations are expanded into a Fourier series, and the differential equation of successive harmonics of each state variable is derived. With the help of this differential equation, the power against different phase-shift ratios is calculated. By keeping these [46,47] as reference, an average modeling for the DAB–DC/DC converter is done.

Figure 7 shows the general average model of the DAB–DC/DC converter. With the help of this representation, we can develop a state-space model by using Kirchhoff's voltage law (KVL) and Kirchhoff's current law (KCL). Thus, the DAB–DC/DC converter can be expressed as a linear-time-periodic (LTP) system.

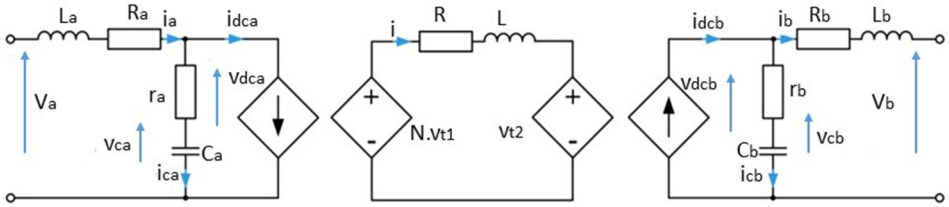


**Figure 7.** Average model of DAB–DC/DC converter.

$$\hat{y} = \emptyset y + f \tag{12}$$

In the above Equation (12), $\emptyset$ denotes the time-varying matrix and can be expressed as

$$\begin{bmatrix} \frac{-RN^2 s_1^2 r_a + s_2^2 r_b}{L} & \frac{N s_1 r_a}{L} & \frac{-s_2 r_b}{L} & \frac{N s_1}{L} & \frac{-s_2}{L} \\ \frac{N s_1 r_a}{L} & \frac{-(R_a + r_a)}{L} & 0 & \frac{-1}{L_a} & 0 \\ \frac{-s_2 r_b}{L_b} & 0 & \frac{-(R_b + r_{b)}}{L} & 0 & \frac{-1}{L_b} \\ \frac{-N S_1}{C_a} & \frac{1}{C_a} & 0 & 0 & 0 \\ \frac{s_2}{C_b} & 0 & \frac{1}{C_b} & 0 & 0 \end{bmatrix} \tag{13}$$

where y is space vector and can be expressed as

$$y = [i \quad i_a \quad i_b \quad v_a \quad v_b]^T \tag{14}$$

The input is

$$f = \begin{bmatrix} 0 & \frac{V_a}{L_a} & -\frac{V_b}{L_b} & 0 & 0 \end{bmatrix}^T \tag{15}$$

In order to perform harmonic analysis, Equations (12) to (15) can be expressed as

$$\hat{y} = \left(A + s_1 B_1 + s_2 B_2 + s_1^2 B_2 + s_1^2 B_4\right) y + f \tag{16}$$

where

$$A = \begin{bmatrix} \frac{-R}{L} & 0 & 0 & 0 & 0 \\ 0 & \frac{-(R_a+r_a)}{L_a} & 0 & \frac{-1}{L_a} & 0 \\ 0 & 0 & \frac{-(R_b+r_b)}{L_b} & 0 & \frac{-1}{L_b} \\ 0 & \frac{1}{C_a} & 0 & 0 & 0 \\ 0 & 0 & \frac{1}{C_b} & 0 & 0 \end{bmatrix} \tag{17}$$

$B1$, $B2$, $B3$, and $B4$ are the $5 \times 5$ matrices, with

$$(B_1)_{1,2} = \frac{Nr_a}{L}, \qquad (B_1)_{2,1} = -\frac{Nr_a}{L_a} \tag{18}$$

$$(B_1)_{1,4} = \frac{N}{L}, \qquad (B_1)_{4,1} = \frac{-N}{C_a} \tag{19}$$

$$(B_2)_{1,3} = -\frac{r_b}{L}, \qquad (B_2)_{3,1} = -\frac{r_b}{L_b} \tag{20}$$

$$(B_5)_{1,2} = -\frac{1}{L}, \qquad (B_2)_{5,1} = \frac{1}{C_b} \tag{21}$$

$$(B_3)_{1,1} = -\frac{N^2 r_a}{L}, \qquad (B_4)_{4,1} = -\frac{r_b}{L} \tag{22}$$

By substituting all other higher-remaining entries with zero, we get

$$u_1 = s_1, \quad u_2 = s_2, \quad u_3 = s_1^2, \quad u_4 = s_2^2,$$

where $U_1$ to $U_4$ are the switching signals. Thus, Equation (16) can be written as

$$\hat{y} = \left(A + \sum_{x=1}^{4} u_x B_x\right) y + f \tag{23}$$

Let us expand $y$ and $u_x$ into a complex trigonometric function

$$y = \sum_{k=-\infty}^{\infty} (y)_k e^{\mathrm{i}wkt} \tag{24}$$

$$u_x = \sum_{k=-\infty}^{\infty} (u_x)_k e^{\mathrm{i}wkt} \tag{25}$$

The Fourier coefficient of the switching signals can be expressed as

$$(u_1)_k = \begin{Bmatrix} 0 & k = 2N \\ \frac{2}{k\pi} \sin\left(\frac{k\varnothing_1}{2}\right) e^{-\frac{\mathrm{i}k\varnothing_1}{2}} & k = 2N+1 \end{Bmatrix} \tag{26}$$

$$(u_2)_k = \begin{Bmatrix} 0 & k = 2N \\ \frac{2}{k\pi} \sin\left(\frac{k\varnothing_2}{2}\right) e^{-\mathrm{i}k(\frac{\varnothing_2}{2}+\varnothing_3)} & k = 2N+1 \end{Bmatrix} \tag{27}$$

$$(u_3)_k = \begin{Bmatrix} \frac{\varnothing_1}{\pi} & k = 2N \\ 0 & k = 2N+1 \\ \frac{2}{k\pi} \sin\left(\frac{k\varnothing_1}{2}\right) e^{-\frac{\mathrm{i}k\varnothing_1}{2}}, & k = 2N \neq 0 \end{Bmatrix} \tag{28}$$

$$(u_4)_k = \begin{Bmatrix} \frac{\varnothing_2}{\pi} & k = 2N \\ 0 & k = 2N+1 \\ \frac{2}{k\pi} \sin\left(\frac{k\varnothing_2}{2}\right) e^{-\mathrm{i}k(\frac{\varnothing_2}{2}+\varnothing_3)}, & k = 2N \neq 0 \end{Bmatrix} \tag{29}$$

From Equation (24), we get

$$\hat{y} = \sum_{k=-\infty}^{\infty} \left(\frac{d}{dt}(y)_k + \mathrm{i}kw(y)_k\right) e^{\mathrm{i}wkt} \tag{30}$$

By putting the value of Equations (24) and (30) into Equation (23), we obtain

$$\sum_{k=-\infty}^{\infty}\left(\frac{d}{dt}(y)_k + \mathrm{i}kw(y)_k\right)e^{\mathrm{i}wkt} = \left(A + \sum_{x=1}^{4}u_x B_x\right)\sum_{k=-\infty}^{\infty}(y_k)e^{\mathrm{i}wkt} + f \tag{31}$$

Simplifying and rearranging Equation (31), we obtain

$$\frac{d}{dt}\,(y)_0 = A(y)_0 + \sum_{x=1}^{4}\left[B_x\sum_{\mathrm{i}}(y)_i(u_x)_{-\mathrm{i}}\right] + f \tag{32}$$

For $k \neq 0$;

$$\frac{d}{dt}\,(y)_k = (A - \mathrm{i}kwI)(y)_k + \sum_{x=1}^{4}\left[B_x\sum_{\mathrm{i}}(y)_{k+i}(u_x)_{-\mathrm{i}}\right] + f \tag{33}$$

$$\frac{dt}{dt}y = Ay + b \tag{34}$$

where

$$y = \begin{bmatrix} (y)_{-N} \\ (y)_{-N}+1 \\ \vdots \\ (y)_{-1} \\ (y)_0 \\ (y)_1 \\ \vdots \\ (y)_{N-1} \\ (y)_N \end{bmatrix}, \quad b = \begin{bmatrix} 0 \\ 0 \\ \vdots \\ 0 \\ f \\ 0 \\ \vdots \\ 0 \\ 0 \end{bmatrix} \tag{35}$$

and $A$ is

$$A = \begin{bmatrix} A_{1,1} & \cdots & A_{1,2N+1} \\ \vdots & \ddots & \vdots \\ A_{2N+1,1} & \cdots & A_{2N+1,N+1} \end{bmatrix} \tag{36}$$

$$A_{p,q} = \left\{ \begin{array}{ll} \sum_{x=1}^{4} B_x\,(u_x)_0 + A + \mathrm{i}(N+1-p)w & for\ \ p = q \\ \sum_{x=1}^{4} B_x(u_x)_{p-q} & for\ \ p \neq q \end{array} \right\} \tag{37}$$

Since Equation (34) is a linear differential equation and the vector b is constant, if the switching frequency is considered constant and all the eigenvalues of matrix $A$ contain negative real parts, then the steady state can be expressed as

$$y_{ss} = \lim_{t->\infty} y(t) = -A^{-1}b \tag{38}$$

By using Equation (38), we can get current values $i_a$, $i_b$, and their subsequent harmonic amplitude RMS values. Thus, by simply multiplying these current values with their corresponding DC voltages, $V_a$ and $V_b$, we can calculate the DAB–DC/DC converter power against different phase-shift ratios. Furthermore, once we get complex magnitudes of harmonics, we can also draw the wave forms of space vector y in the time domain with the help of Equation (24).

Small-Signal Analysis

In the above section, a generalized average mathematic model is discussed to do steady-state analysis of the DAB–DC/DC converter. Now, we will do the small-signal analysis of the DAB–DC/DC converter at steady state to investigate the effect of perturbations on the transmitted power.

Since the desired phase-shift angle in the proposed FCC technique is calculated from the controller Equation (10) and is independent of the PI current controller, and as the PI

controller is implemented to compensate for the existing error between a mathematical equation and a real system, therefore, the system stability is not affected by the PI controller parameters and primarily depends on the sampled input voltage, output, and load current used in the mathematical Equation (10) for calculating the phase-shift ratio. Sensors and their interfacing circuits are the main source for causing disturbances in the sampled voltages and current. Therefore, a small-signal analysis is done at steady state to investigate the effect of disturbances on the transmitted power.

Assume a small-signal disturbance $\widetilde{V}$ in occurs in the input voltage, while the output load current is sampled accurately. As this small-signal disturbance $\widetilde{V}$ in is very small, the calculated phase-shift ratio $\overline{D}_{V_{in}}$ can be written as [48]

$$\overline{D}_{V_{in}} = D + \widetilde{D} = D + \frac{\partial D}{\partial V_{in}} \widetilde{V}_{in} \tag{39}$$

From Equation (10), the partial derivative of the phase-shift ratio $D$ with reference to $V_{in}$ is

$$\frac{\partial D}{\partial V_{in}} = \frac{I_{o_{ref}} I_*}{I_{out}\left(\sqrt{1/4 - 2I_{o_{ref}} I_* V_{in}/I_{out}}\right)} \tag{40}$$

Moreover, the transmitted power can be expressed as

$$\overline{P} = P + \Delta P = V_{out}(V_{in} + \widetilde{V}_{in})\left(D + \widetilde{D}\right)[1 - (D + \widetilde{D})]/2 \tag{41}$$

$\Delta P$ is the ripples in the transmitted power, and by simplifying and ignoring the higher order perturbations, the transmitted power can be written as

$$\overline{P} = P + \Delta P \approx V_{in} V_{out} D(1 - D)/2 + \frac{V_{out}(V_{in}\widetilde{D} + D\widetilde{V}_{in} - 2V_{in}D\widetilde{D} - D^2\widetilde{V}_{in})}{2} \tag{42}$$

Thus, ΔP can be expressed as

$$\Delta P \approx V_{out}(V_{in}\widetilde{D} + D\widetilde{V}_{in} - 2V_{in}D\widetilde{D} - D^2\widetilde{V}_{in})/2 \tag{43}$$

By putting the value of $\widetilde{D}$ from Equation (13) and simplifying Equation (16), the ripples in the transmitted power generated due to small signal perturbation $\widetilde{V}_{\text{in}}$ can then be further written as

$$\Delta P \approx \left(\frac{I_{o_{ref}} I_* V_{out}}{I_{out}\left(\sqrt{1/4 - 2I_{o_{ref}} I_* V_{in}/I_{out}}\right)} + DV_{out}\right)\widetilde{V}_{in} - \left(\frac{2DI_{o_{ref}} I_* V_{out} V_{in}}{I_{out}\left(\sqrt{1/4 - 2I_{o_{ref}} I_* V_{in}/I_{out}}\right)} - D^2 V_{out}\right)\widetilde{V}_{in} \tag{44}$$

Similarly, assume a small-signal disturbance $\widetilde{I}_{out}$ occurred in the output load current, whereas the sampled input voltage is correct. The partial derivative of the phase-shift ratio $D$ with reference to $I_{out}$ can be written as

$$\frac{\partial D}{\partial I_{out}} = \frac{-I_{o_{ref}} I_* V_{in}}{I^2_{out}\left(\sqrt{1/4 - 2I_{o_{ref}} I_* V_{in}/I_{out}}\right)} \tag{45}$$

The ripples in the transmitted power generated due to small-signal perturbation $\widetilde{I}_{out}$ can be written as

$$\Delta P \approx \left(\frac{-(1 - 2D) I_{o_{ref}} I_* V_{in}}{2I^2_{out}\left(\sqrt{1/4 - 2I_{o_{ref}} I_* V_{in}/I_{out}}\right)}\right)\widetilde{I}_{out} \tag{46}$$

Hence, the total ripples in the transmitted power produced due to the perturbations in the input voltage and output current can be obtained by combing Equations (44) and (46)

$$\Delta P_{total} \approx \left(\frac{I_{o_{ref}} I_* V_{out}}{I_{out}\left(\sqrt{1/4-2I_{o_{ref}} I_* V_{in}/I_{out}}\right)} + DV_{out}\right)\widetilde{V}_{in} - \left(\frac{2DI_{o_{ref}} I_* V_{out} V_{in}}{I_{out}\left(\sqrt{1/4-2I_{o_{ref}} I_* V_{in}/I_{out}}\right)} - D^2 V_{out}\right)\widetilde{V}_{in} - \left(\frac{(1-2D) I_{o_{ref}} I_* V_{in}}{2I^2_{out}\left(\sqrt{1/4-2I_{o_{ref}} I_* V_{in}/I_{out}}\right)}\right)\widetilde{I}_{out} \quad (47)$$

From Equation (47), it can be seen that to minimize the output power ripple of the DAB–DC/DC converter, the load current, the input, and output voltage should be sampled precisely. A large capacitor at the output side of the DAB–DC/DC can be used to minimize these sampling effects on the output power due to these perturbations in the sampling voltage and currents. However, it would increase the overall weight and size of the DC/DC converter. Thus, a controller should be dynamic enough to tackle these perturbations and track the desired power swiftly.

## 4. MATLAB Simulation Results and Discussion

The proposed fast current controller is implemented on a 500 W DAB–DC/DC converter. The electrical specifications of the DAB–DC/DC converter are shown in Table 1. To verify the effectiveness and the aforesaid theoretical analysis, this 500 W constant-current-based DAB–DC/DC converter is modeled and simulated in MATLAB/Simulink software. The block diagram of the simulations and flow of signals for the FCC, LCFF, MBPS, and PI controllers are shown in Figure 8. Four test cases, the tracking of the reference current during the startup process, a sudden change in the load, a change in the input voltage variation, and a change in the desired output current, are simulated. Furthermore, the proposed fast current controller (FCC) is compared with the MBPS, LCFF, and the traditional PI current controller.

**Table 1.** DAB–DC/DC electrical specifications used for MATLAB simulation.

| System Parameters | Value |
|---|---|
| Power | 500 W |
| Input voltage | 100 V |
| Switching frequency | 20 kHz |
| Transformer turn ratio | 1:1 |
| Total inductance | 112 µH |
| Input capacitor | 220 µF |
| Output capacitor | 130 µF |
| Rated resistive load | 20 Ω |

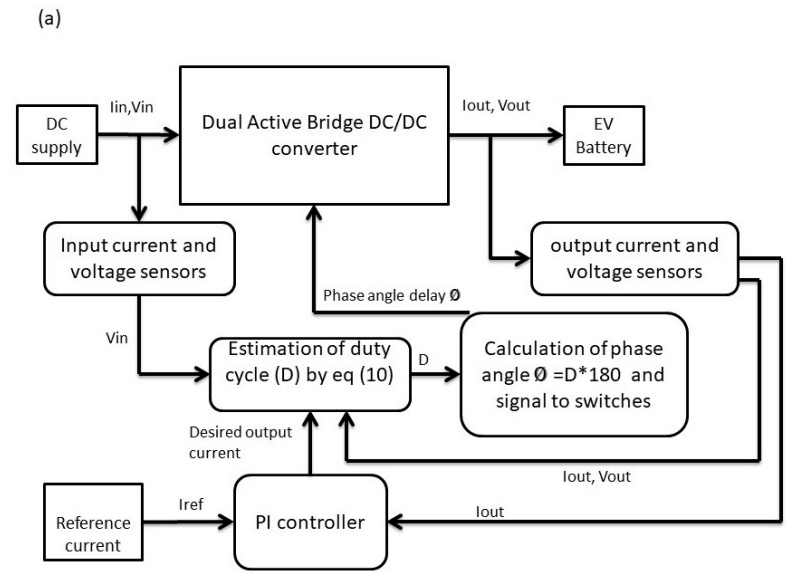


**Figure 8.** *Cont.*

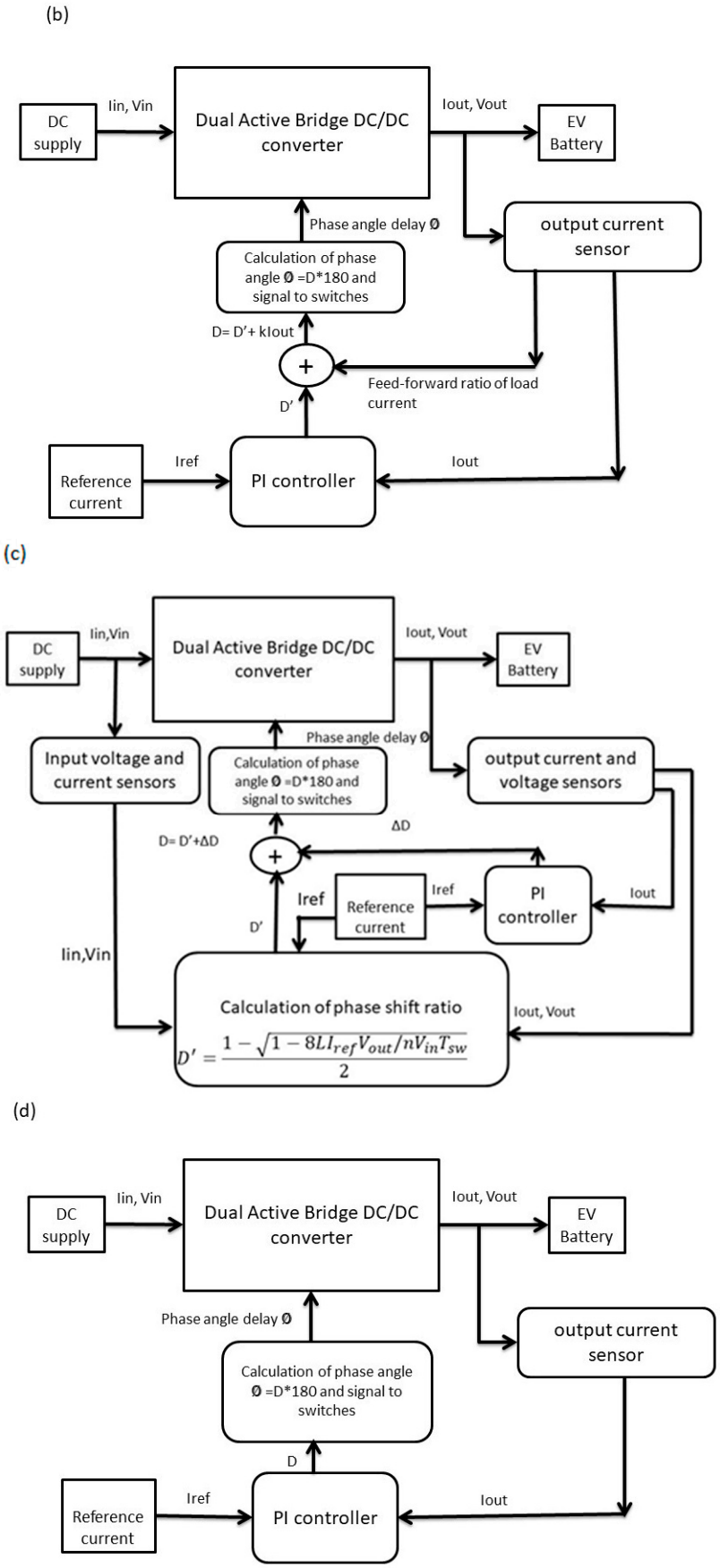


**Figure 8.** Block diagram of control schemes: (**a**) FCC; (**b**) LCFF; (**c**) MBPS; (**d**) PI.

### *4.1. Case1: Tracking 5A Reference Current during Startup*

During the startup process, an output current of 5 A is set as a reference current. As shown in Figure 9, it took 25 ms to charge the output capacitor and reach the desired 5 A output current with the proposed FCC scheme. The MBPS control scheme took 155 ms to reach the steady state while the LCFF and PI current controller tracked the desired output current in 635 ms and 820 ms with an overshoot of 2 A and 1.7 A, respectively. From Figure 9, it can be seen that the proposed FCC has achieved the steady state in the shortest time, whereas the conventional PI controller took the longest duration.

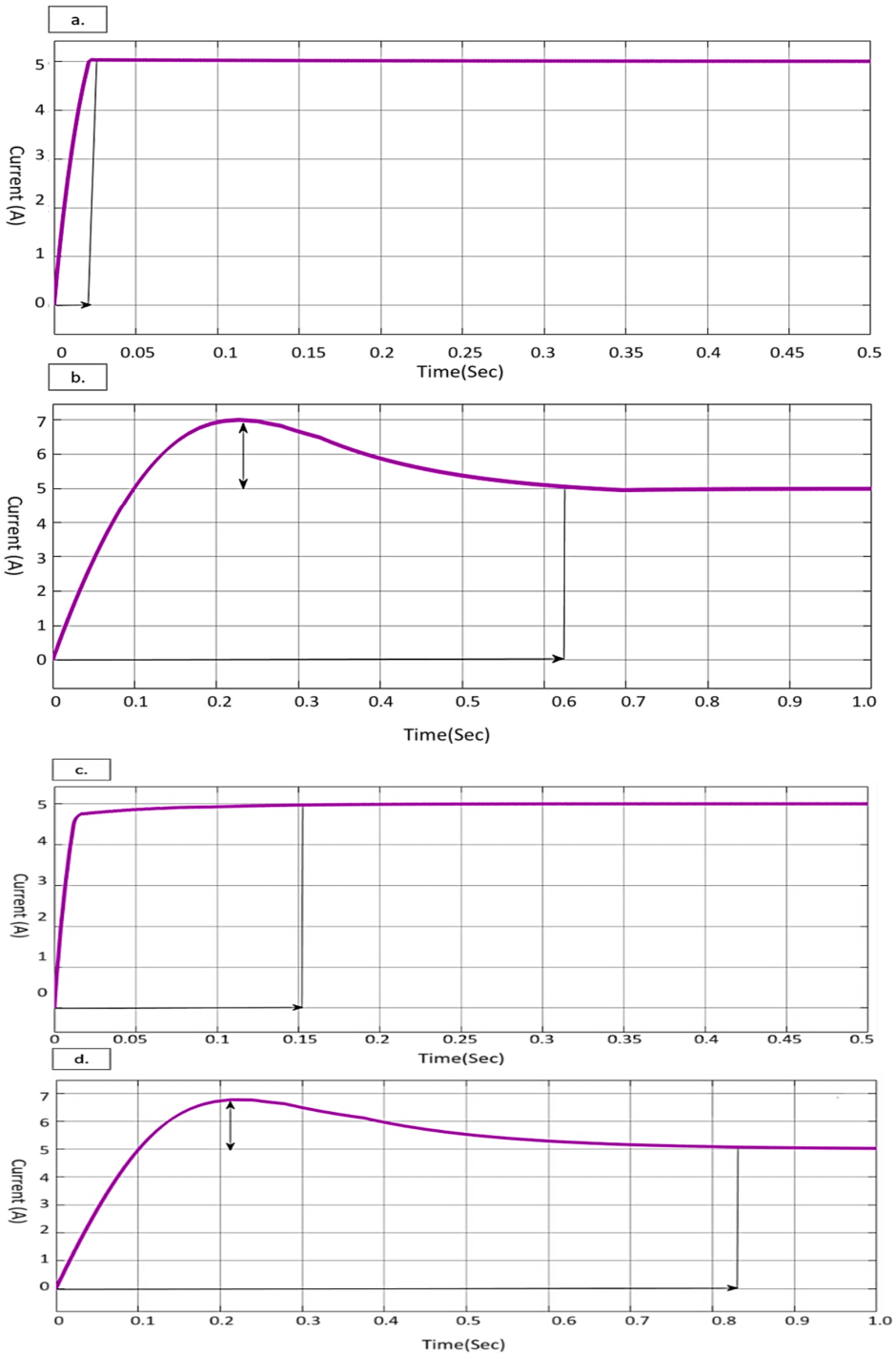


**Figure 9.** Simulation results during startup and tracking 5 A reference current: (**a**) FCC; (**b**) LCFF; (**c**) MBPS; (**d**) PI.

### *4.2. Case2: Change in Reference Current*

As shown in Figure 10, the converter was working normally and giving the reference current of 5 A, and suddenly at 1 s, the desired output current changed to 2.5 A. With this change in the reference current, the proposed FCC tracked the new reference output current swiftly in 65 ms. With the MBPS control scheme, it took 160 ms to track the new reference current, while the LCFF and PI current controller tracked the new desired output current in 580 ms and 635 ms with an undershoot of approximately 0.3 A and 0.2 A, respectively. Thus, the comparison has shown that the proposed FCC has the shortest settling time.

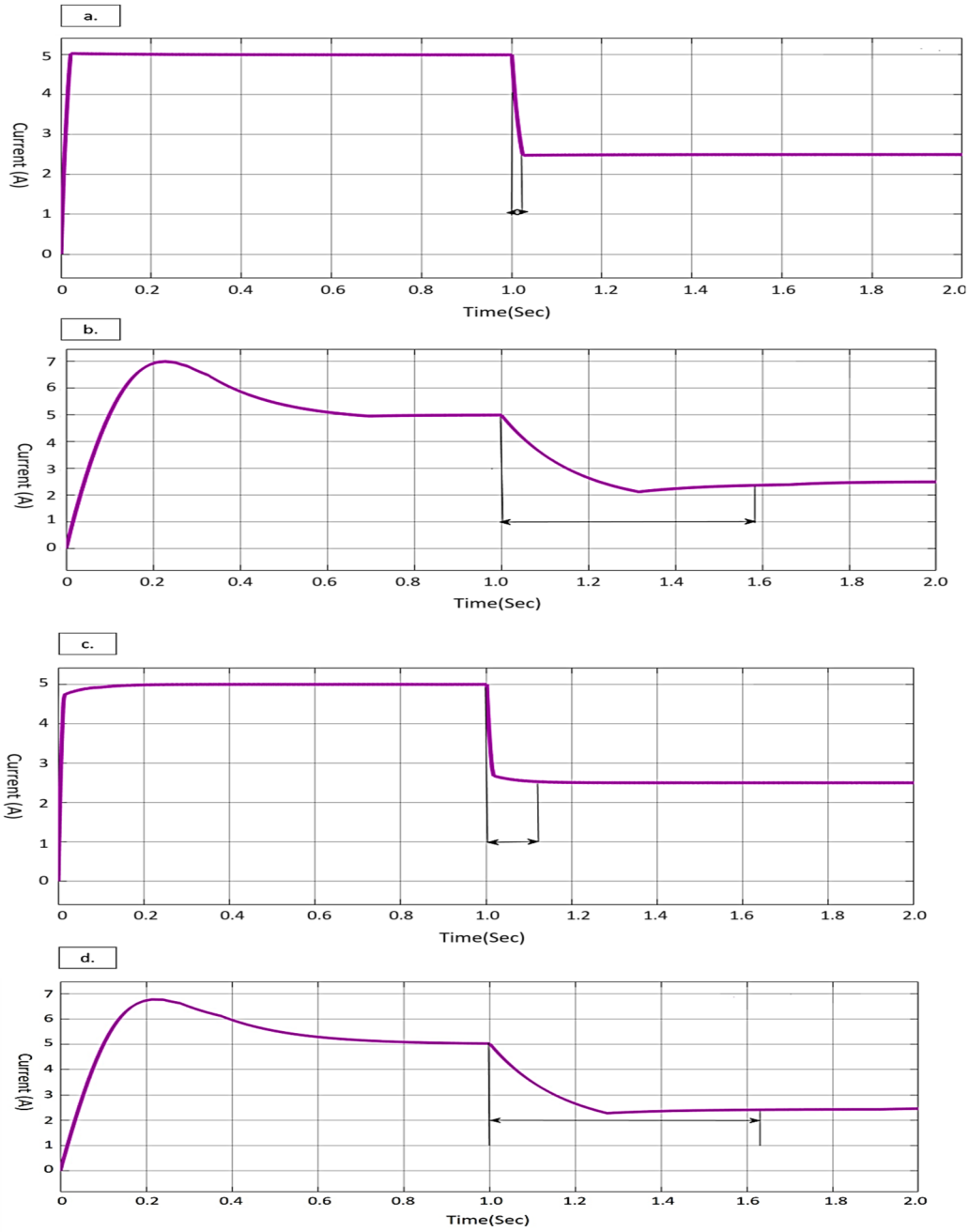


**Figure 10.** Simulation results when reference current changes from 5 A to 2.5 A after 1 s: (**a**) FCC; (**b**) LCFF; (**c**) MBPS; (**d**) PI.

### *4.3. Case3: Change in Load*

Two test scenarios are considered for this test case, i.e., 25% and 50% change in the load resistance. As shown in Figure 11, the system was running normally at the maximum

rated load resistance of 20 Ω, and after 1 s, there was a 25% change in the load resistance (20 Ω to 15 Ω). Due to this 25% change in the load, the settling time for the PI controller is 240 ms with a maximum overshoot of 1.6 A. In the case of the LCFF, the settling time is 380 ms with a maximum overshoot of 1.4 A. With the MBPS controller, the settling time is 90 ms with a maximum overshoot of 0.3 A, whereas the proposed FCC tracked the reference current in shortest settling time of 9 ms with a maximum overshoot of 0.4 A.

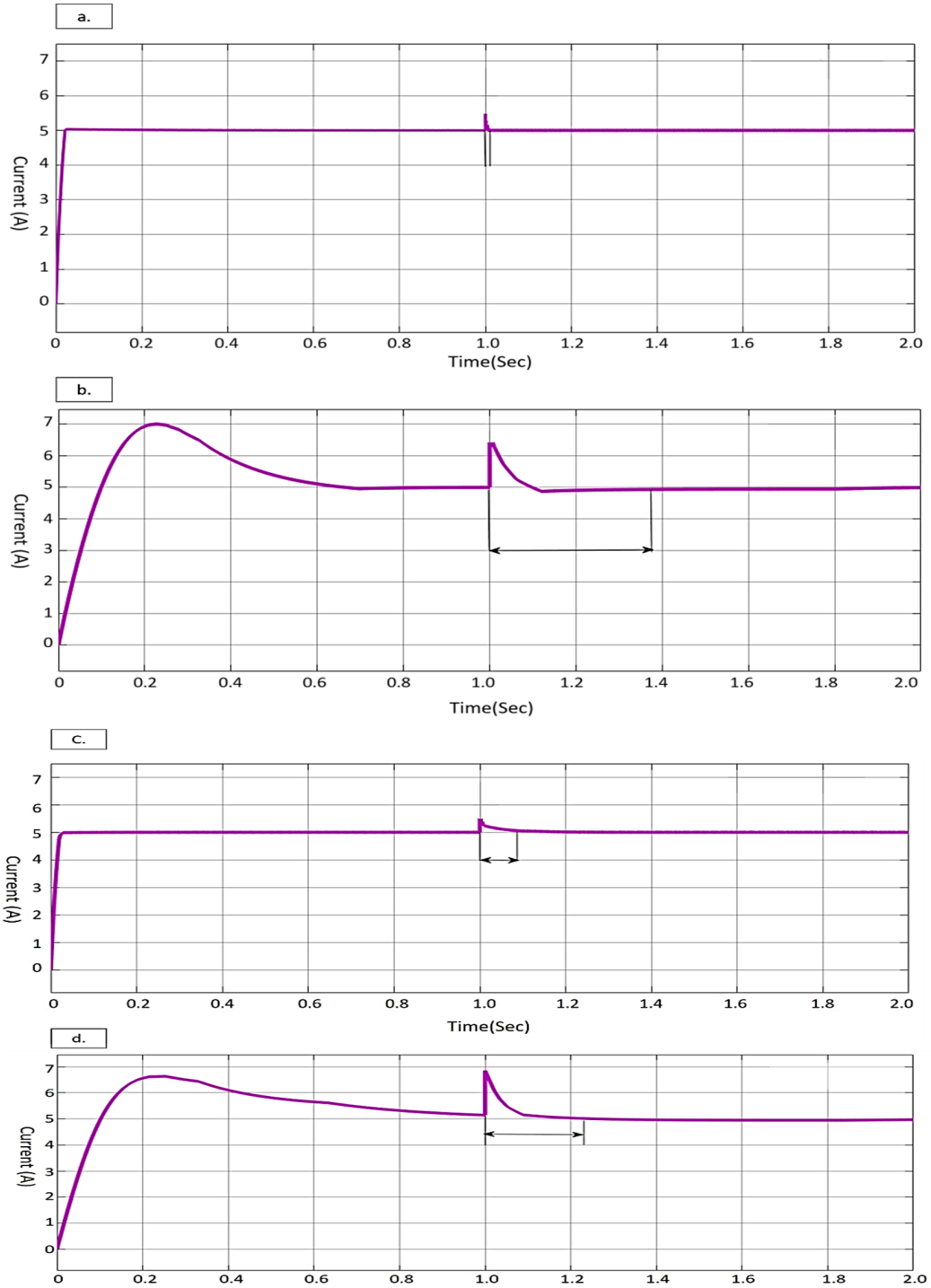


**Figure 11.** Simulation results when there is a 25% change in load resistance (20 Ω to 15 Ω): (**a**) FCC; (**b**) LCFF; (**c**) MBPS; (**d**) PI.

In the second scenario, again, the system was running normally at a rated maximum load resistance of 20 Ω; however, this time, the load resistance changed to 50% (20 Ω to 10 Ω)

after 1 s, as shown in Figure 12. Due to this 50% change in the load resistance, the settling time for the PI controller is 630 ms with a maximum overshoot of 5 A. In the case of the LCFF, the settling time is 600 ms with a maximum overshoot of 4.2 A. With the MBPS controller, this settling time is 80 ms with a maximum overshoot of 0.7 A, whereas, again, the proposed FCC tracked the reference current in shortest settling time of 15 ms with a maximum overshoot of 0.9 A. Thus, this test case validates that, under load-resistance variation, the proposed FCC has the fastest dynamic response and tracked the desired output current in the shortest time, while the PI controller has the slowest dynamic response.

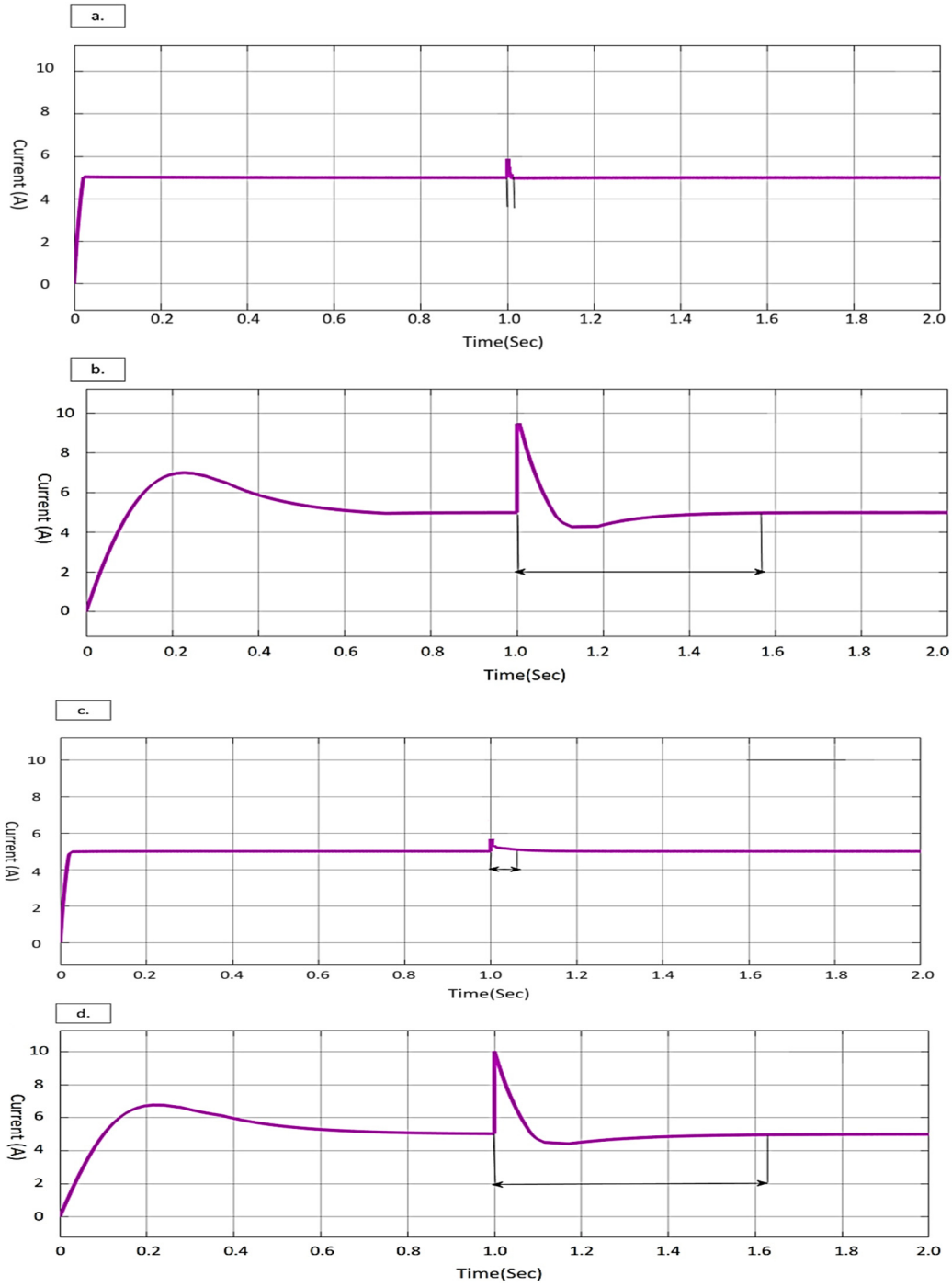


**Figure 12.** Simulation results when there is a 50% change in load resistance (20 Ω to 10 Ω): (**a**) FCC; (**b**) LCFF; (**c**) MBPS; (**d**) PI.

### *4.4. Case4: Variation in the Input Voltage*

In this test case, two possible scenarios are considered, i.e., a decrease in system input voltage and an increase in system input voltage. In the first scenario, the system was running normally at 100 V input voltage. However, at 1 s, there was an abrupt change in the system input voltage (input voltage reduced from 100 V to 85 V) that was introduced, as shown in Figure 13. Due to this abrupt change, the settling time for the PI controller is 500 ms with a maximum undershoot of 0.4 A. In the case of the LCFF, the settling time is 410 ms with a maximum undershoot of 0.3 A. However, the proposed FCC and MBPS control strategies have a negligible effect on performance due to a decrease in the input voltage. In the second scenario, again, the system was running normally at 100 V input, and an abrupt change in the system input voltage was introduced. However, this time, the input voltage increased from 100 V to 115 V, as shown in Figure 14. Due to this abrupt change in the input voltage, the settling time for the PI controller is 462 ms with a maximum undershoot of 0.2 A. In the case of the LCFF, the settling time is 220 ms with a maximum overshoot of 0.3 A. Again, the proposed FCC and MBPS control strategies have a negligible effect on performance due to an increase in the input voltage. The simulation results are summarized in Table 2; from the results, it can be concluded that the proposed current controller is very effective and has a very fast dynamic response against various disturbances compared to the other three controllers.

**Table 2.** Summary of MATLAB simulation results.

| Test Cases | FCC | | LCFF | | MBPS | | PI | |
|---|---|---|---|---|---|---|---|---|
| | **Δt** | **Δi** | **Δt** | **Δi** | **Δt** | **Δi** | **Δt** | **Δi** |
| 5 A (ref) | 25 ms | -/- | 635 ms | 2 A (overshoot) | 155 ms | -/- | 820 ms | 1.7 A (overshoot) |
| 5 A to 2.5 A (ref) | 65 ms | -/- | 580 ms | 0.3 (undershoot) | 160 ms | -/- | 635 ms | 0.2 (undershoot) |
| 25% Load change | 9 ms | 0.4 A | 380 ms | 1.4 A | 90 ms | 0.3 A | 240 ms | 1.6 A |
| 50% Load change | 15 ms | 0.9 A | 600 ms | 4.2 A | 80 ms | 0.7 A | 630 ms | 5 A |
| Input voltage change (100 V to 85 V) | Neg. | -/- | 410 ms | 0.3 A | Neg. | -/- | 500 ms | 0.4 A |
| Input voltage change (100 V to 115 V) | Neg. | -/- | 220 ms | 0.3 A | Neg. | -/- | 462 ms | 0.2 A |

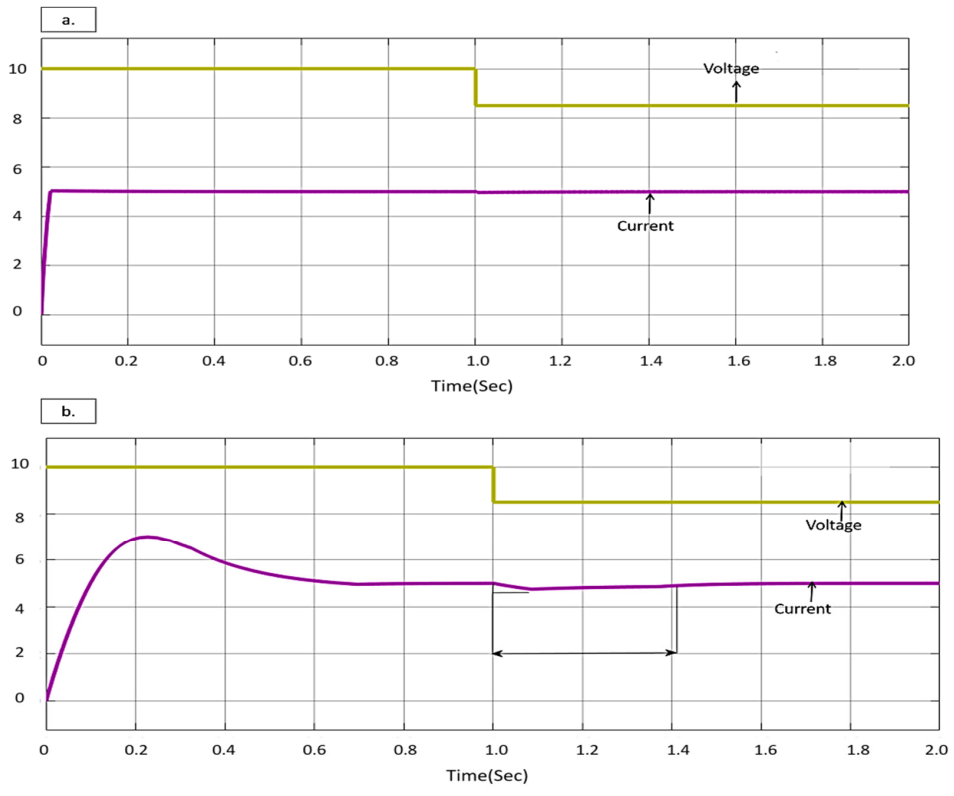


**Figure 13.** *Cont.*

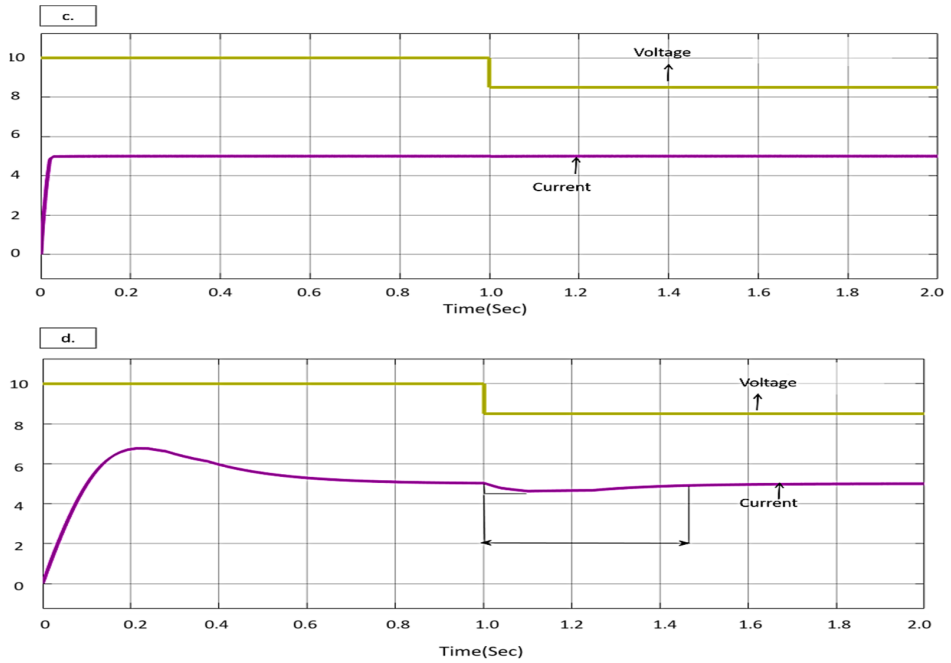


**Figure 13.** Simulation results during input voltage step-down (100 V to 85 V voltage scaling 1 box = 20 V): (**a**) FCC; (**b**) LCFF; (**c**) MBPS; (**d**) PI.

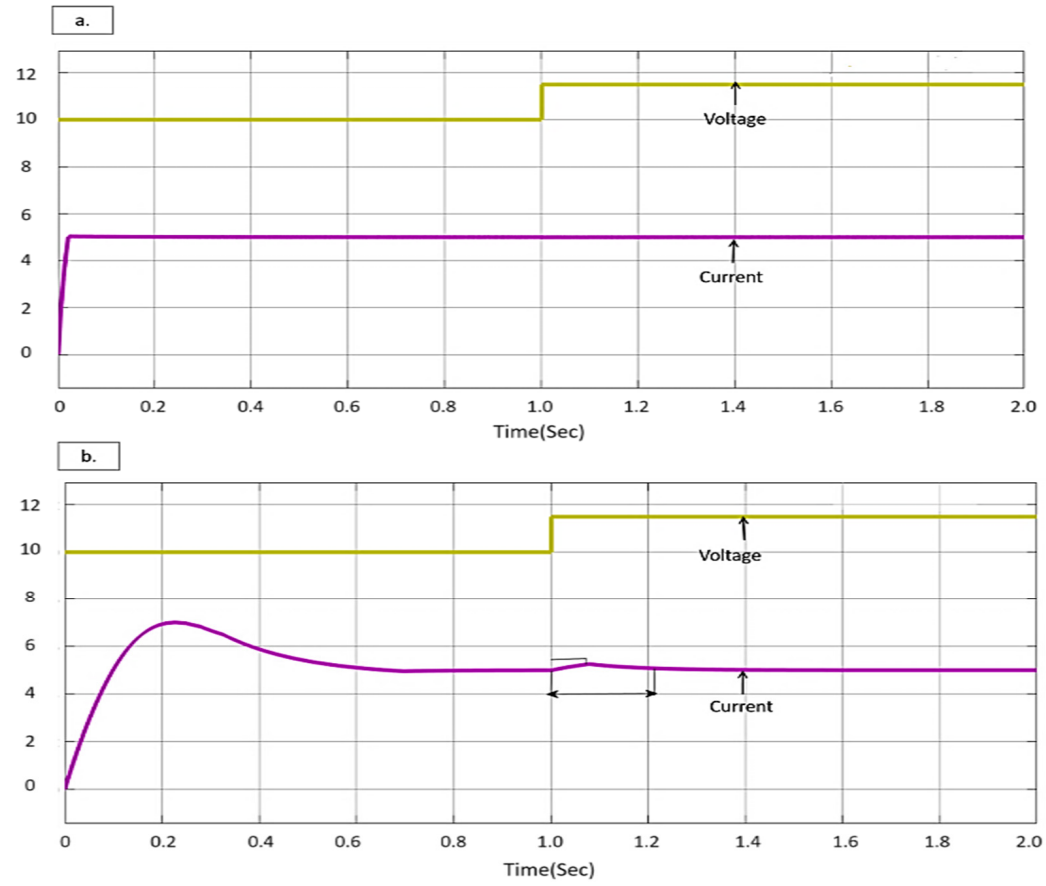


**Figure 14.** *Cont.*

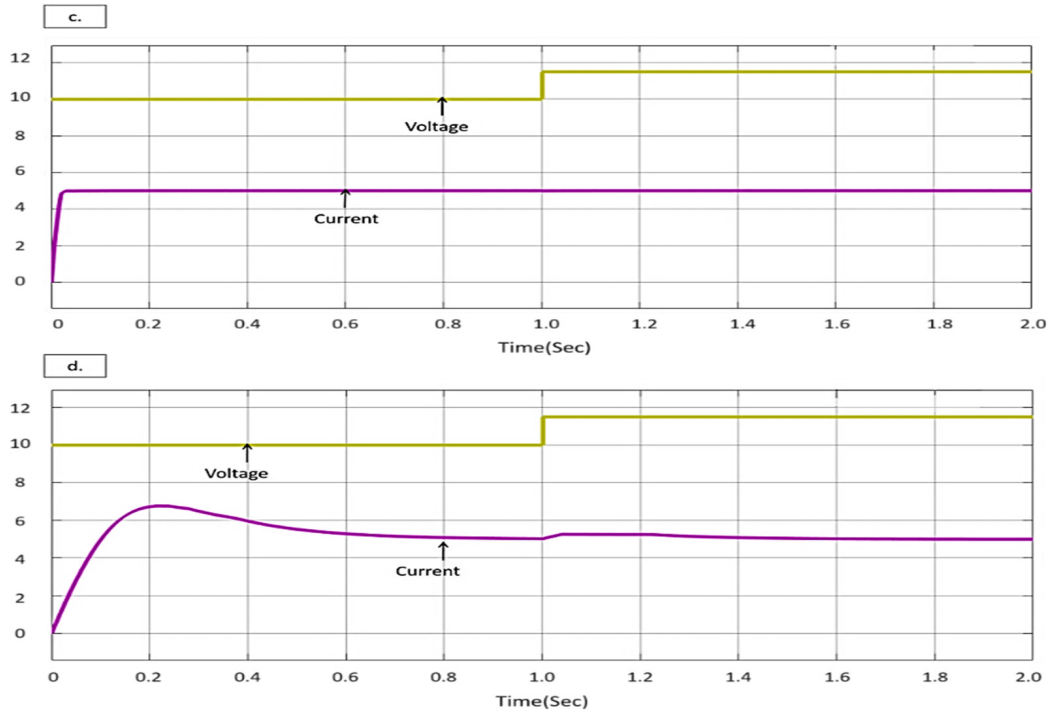


**Figure 14.** Simulation results during input voltage step-up (100 V to 115 V voltage scaling 1 box = 20 V): (**a**) FCC; (**b**) LCFF; (**c**) MBPS; (**d**) PI.

## 5. Experimental Results and Discussion

To verify the effectiveness of the proposed current controller, a scaled-down 300 W lab prototype DAB–DC/DC converter is designed with the TMS320F28335 DSP controller of Texas Instruments, as shown in Figure 15. The electrical parameters of the prototype are listed in Table 3.

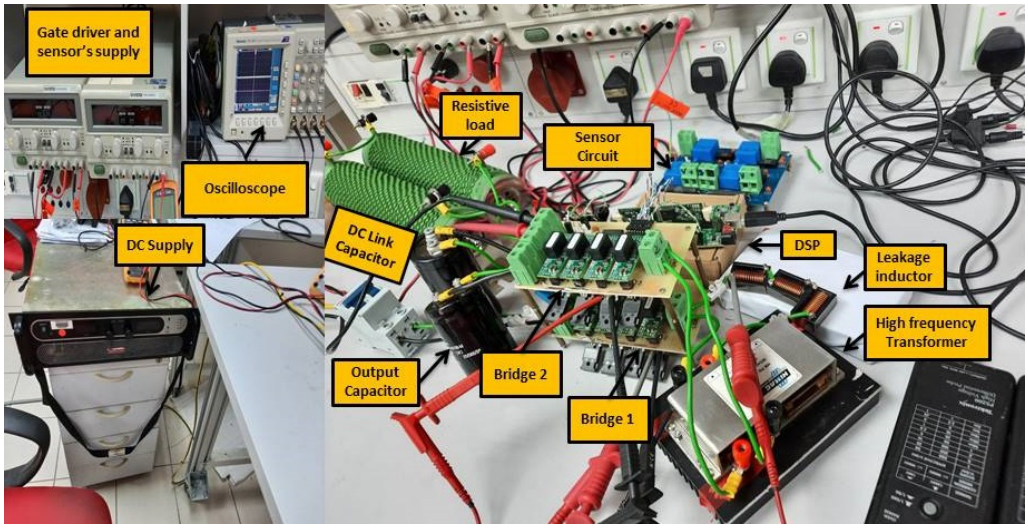


**Figure 15.** Experimental setup of 300 W DAB–DC/DC converter.

During the startup process, an output current of 4 A is set as a reference current. As shown in Figure 16, it took 30 ms to charge the output capacitor and reach the desired 4 A output current with the proposed FCC scheme. The MBPS control scheme took 55 ms to reach the steady state, while the LCFF and PI current controller tracked the desired output current in 160 ms and 280 ms, respectively. From Figure 16, it can be seen that the proposed

FCC has attained a steady state in the shortest time, whereas the conventional PI controller took the longest duration.

**Table 3.** DAB–DC/DC electrical specifications used for Lab prototype.

| System Parameters | Value |
|---|---|
| Power | 300 W |
| Input voltage | 75 V |
| Switching frequency | 20 kHz |
| Transformer turn ratio | 1:1 |
| Total inductance | 55 μH |
| Input capacitor | 220 μF |
| Output capacitor | 220 μF |
| Resistive load | 20–30 Ω |
| Desired output current | 4 A |

Figures 17 and 18 show the transient experimental results of the DAB–DC/DC converter when there is variation in the system input voltage. From Figure 17, it can be seen that the system was running normally at the rated input voltage. However, suddenly an abrupt change in the system input voltage (input voltage reduced from 75 V to 65 V) was introduced. Due to this abrupt change, the settling time for the PI controller is 210 ms with a maximum undershoot of 0.35 A. In the case of the LCFF, the settling time is 170 ms with a maximum undershoot of 0.3 A. However, the proposed FCC and MBPS control strategies have a negligible effect on performance due to a decrease in the input voltage. Similarly, Figure 18 shows that the system is running normally at 65 V, and an abrupt change in the system input voltage is introduced. However, this time the input voltage increased from 65 V to 75 V. Due to this abrupt change in the input voltage, the settling time for the the PI controller is 290 ms with a maximum overshoot of 0.2 A. In the case of the LCFF, the settling time is 240 ms with a maximum overshoot of 0.2 A. Again, the proposed FCC and MBPS control strategies have a negligible effect on performance due to an increase in the input voltage.

Figures 19 and 20 show the transient experimental results of the DAB–DC/DC converter when there is variation in the load resistance, i.e., 25% and 50% change in the load resistance. From Figure 19, it can be seen that the system is running normally at the rated load resistance of 20 Ω, and suddenly there was a 25% change in the load resistance (20 Ω to 25 Ω). Due to this 25% change in the load, the settling time for the PI controller is 560 ms with a maximum overshoot of 0.75 A. In the case of the LCFF, the settling time is 490 ms with a maximum overshoot of 0.55 A. With the MBPS controller, the settling time is 220 ms with a maximum overshoot of 0.4 A, whereas the proposed FCC tracked the reference current in shortest settling time of 150 ms with a maximum overshoot of 0.3 A. In the second scenario, again, the system was running normally at load resistance of 20 Ω; however, this time load resistance was changed to 50% (20 Ω to 30 Ω), as shown in Figure 20. Due to this 50% change in the load, the settling time for the PI controller is 1420 ms with a maximum overshoot of 1.2 A. In the case of the LCFF, the settling time is 1050 ms with a maximum overshoot of 1 A. With the MBPS controller, this settling time is 410 ms with a maximum overshoot of 0.6 A, whereas, again, the proposed FCC tracked the reference current in shortest settling time of 290 ms with a maximum overshoot of 0.4 A. Thus, this test case validates that, under load resistance variation, the proposed FCC has the fastest dynamic response and tracked the desired output current in the shortest time, while the PI controller has the slowest dynamic response. The experimental results are summarized in Tables 4 and 5. From the results, it can be concluded that the proposed current controller is very effective and has very fast dynamic response against various disturbances compared to the other three controllers.

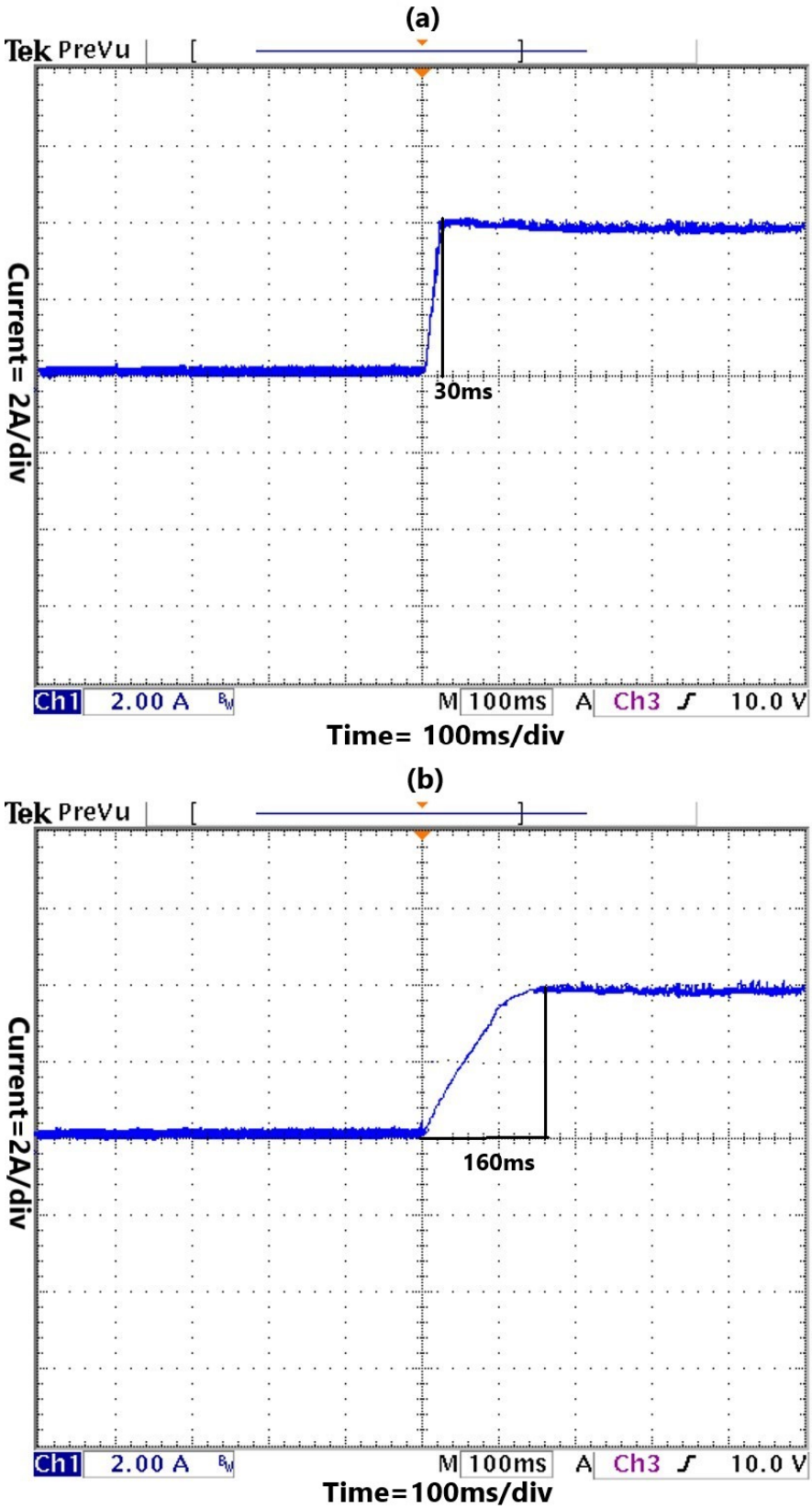


**Figure 16.** *Cont*.

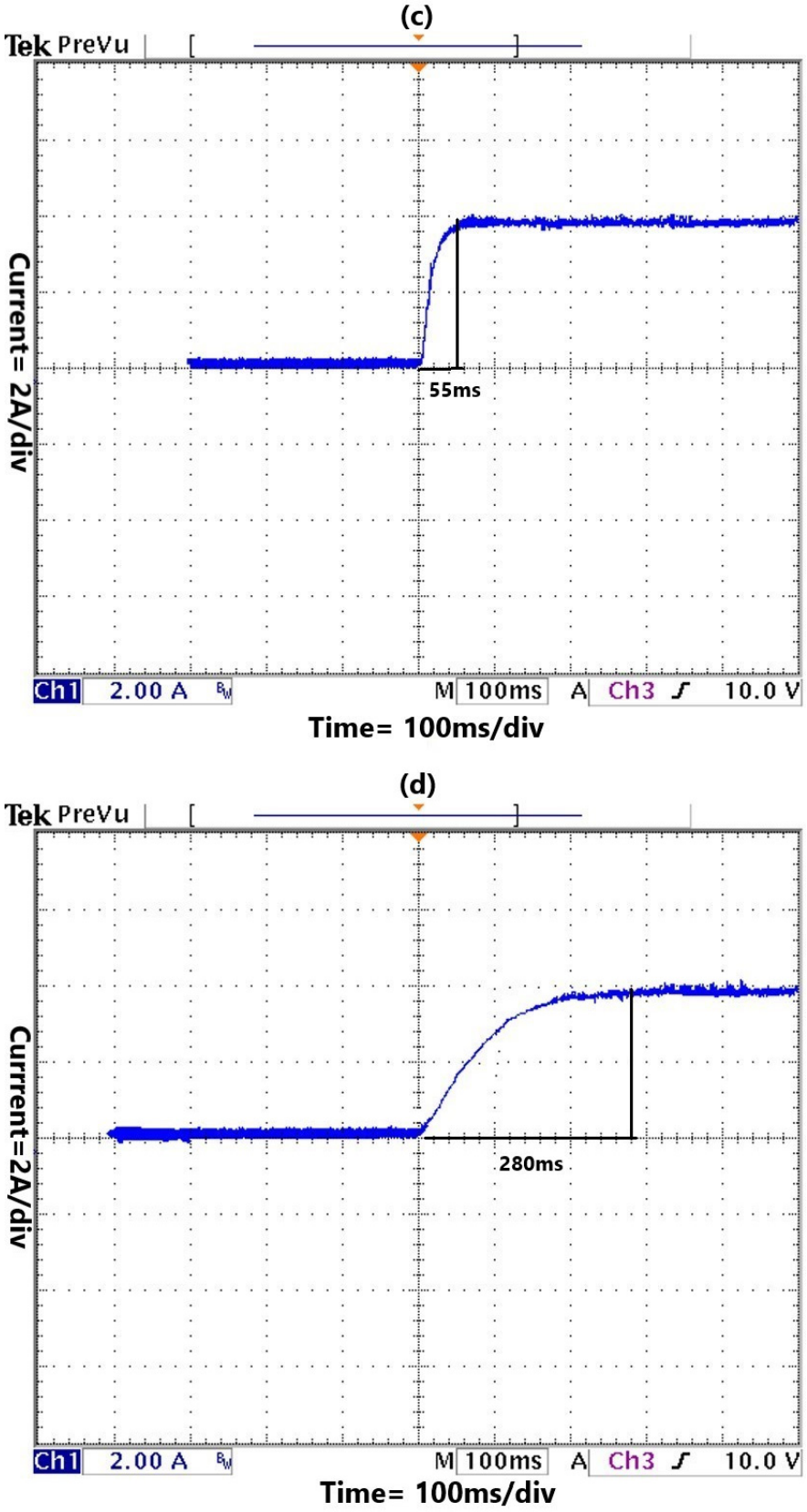


**Figure 16.** Experimental results during startup and tracking 4 A reference current: (**a**) FCC; (**b**) LCFF; (**c**) MBPS; (**d**) PI.

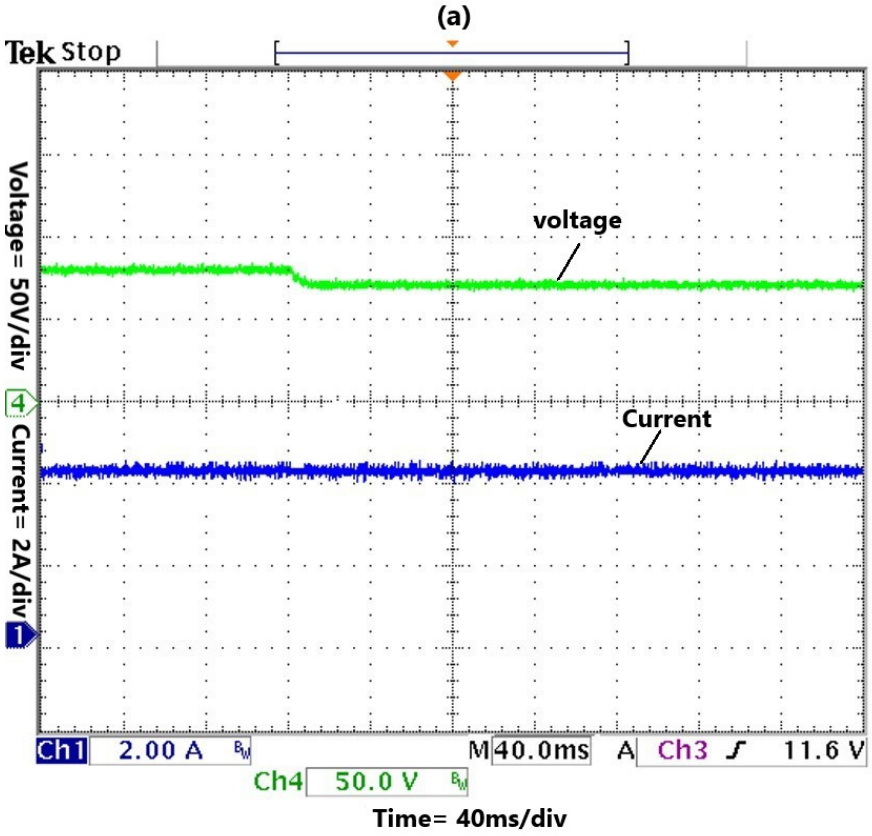


**Figure 17.** *Cont*.

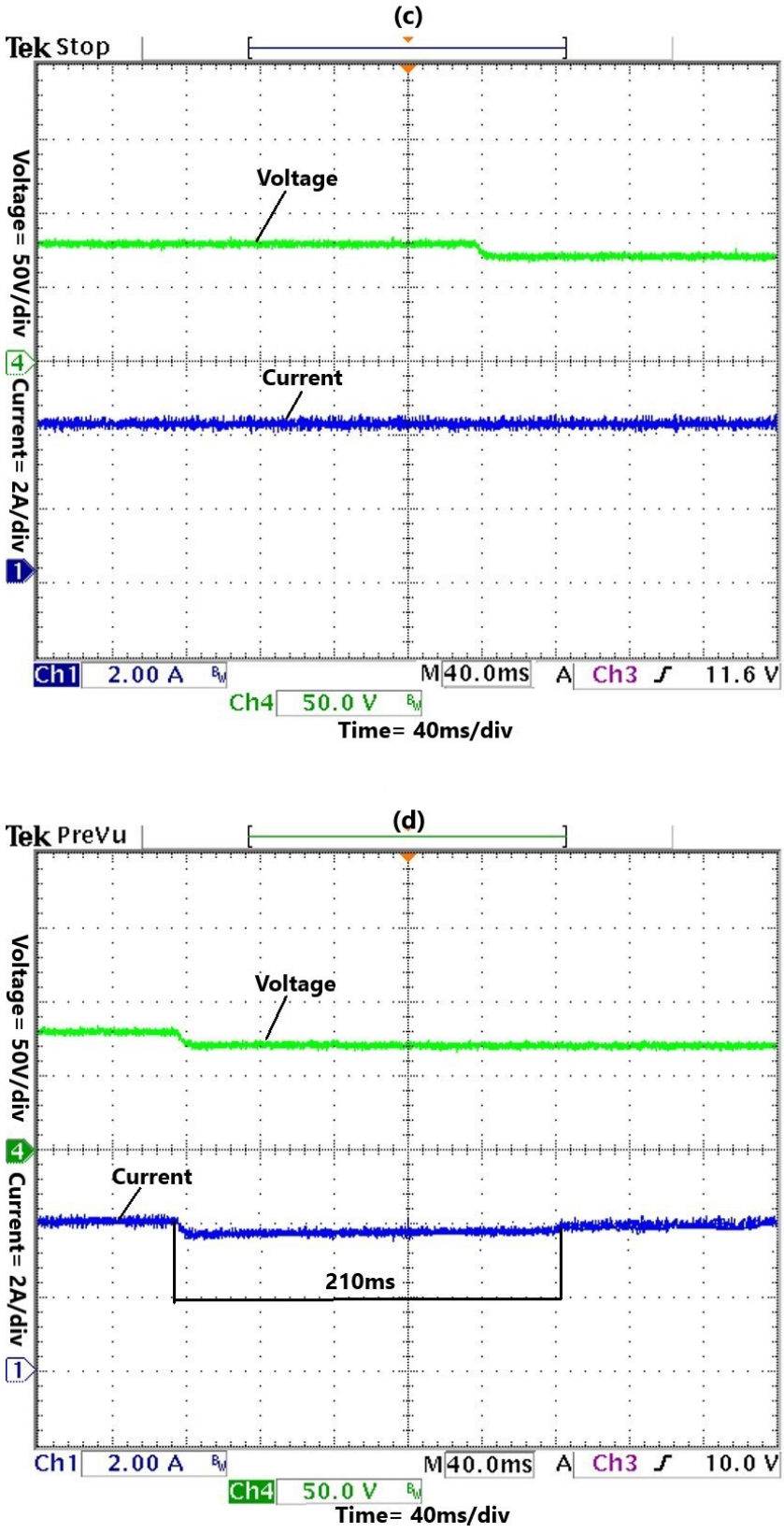


**Figure 17.** Experimental results during input voltage step-down (75 V to 65 V): (**a**) FCC; (**b**) LCFF; (**c**) MBPS; (**d**) PI.

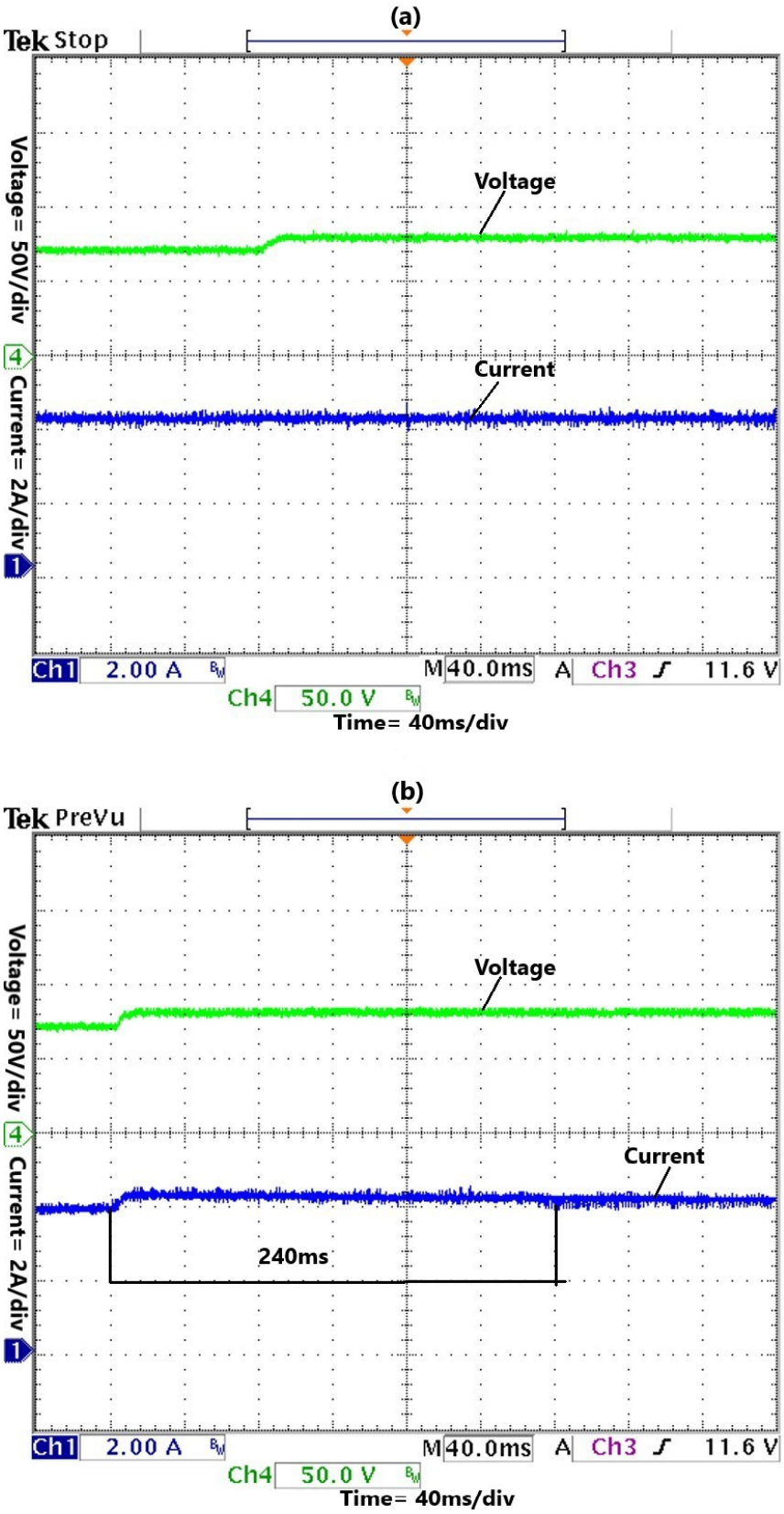


**Figure 18.** *Cont.*

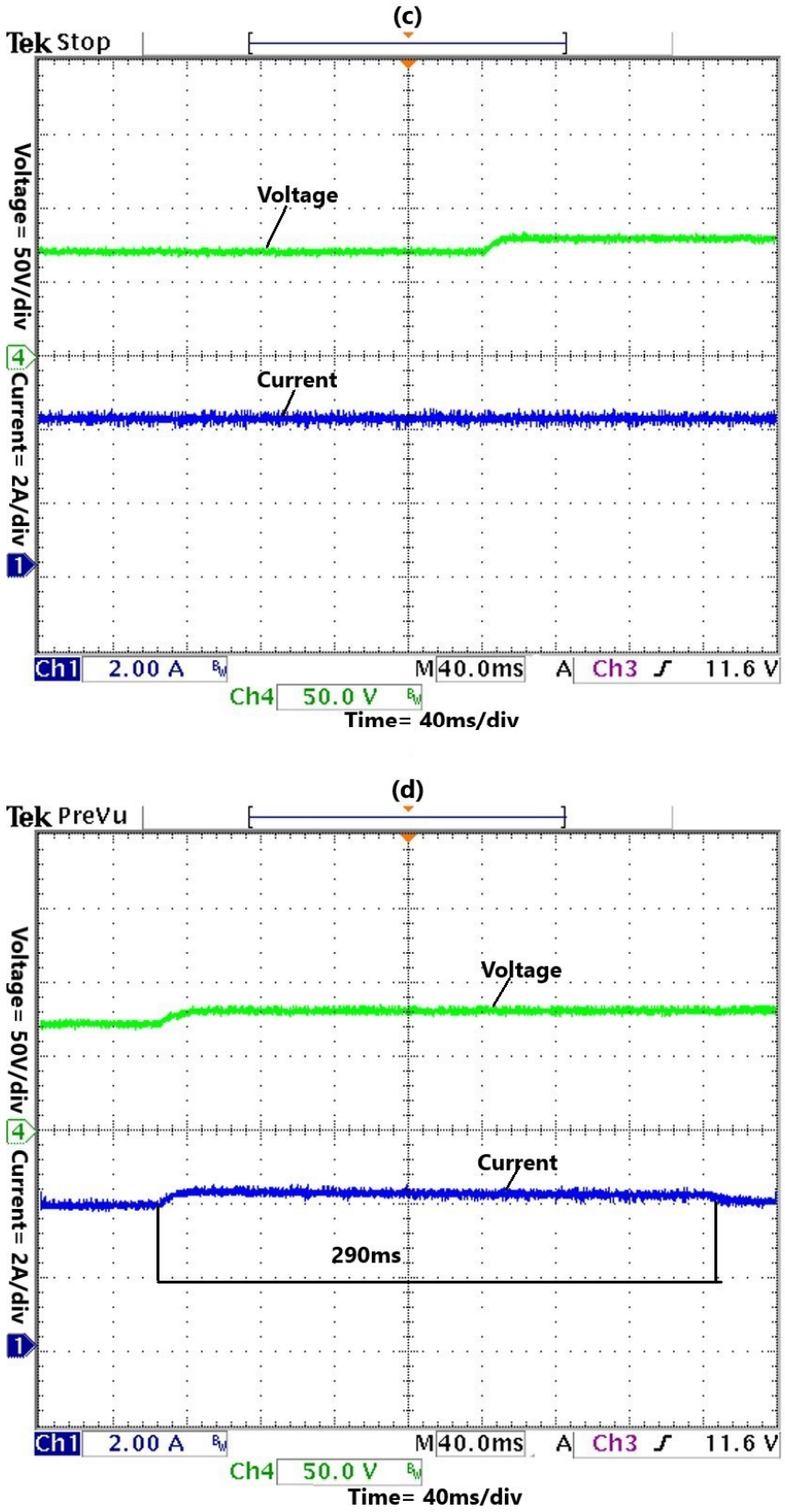


**Figure 18.** Experimental results during input voltage step-up (65 V to 75 V): (**a**) FCC; (**b**) LCFF; (**c**) MBPS; (**d**) PI.

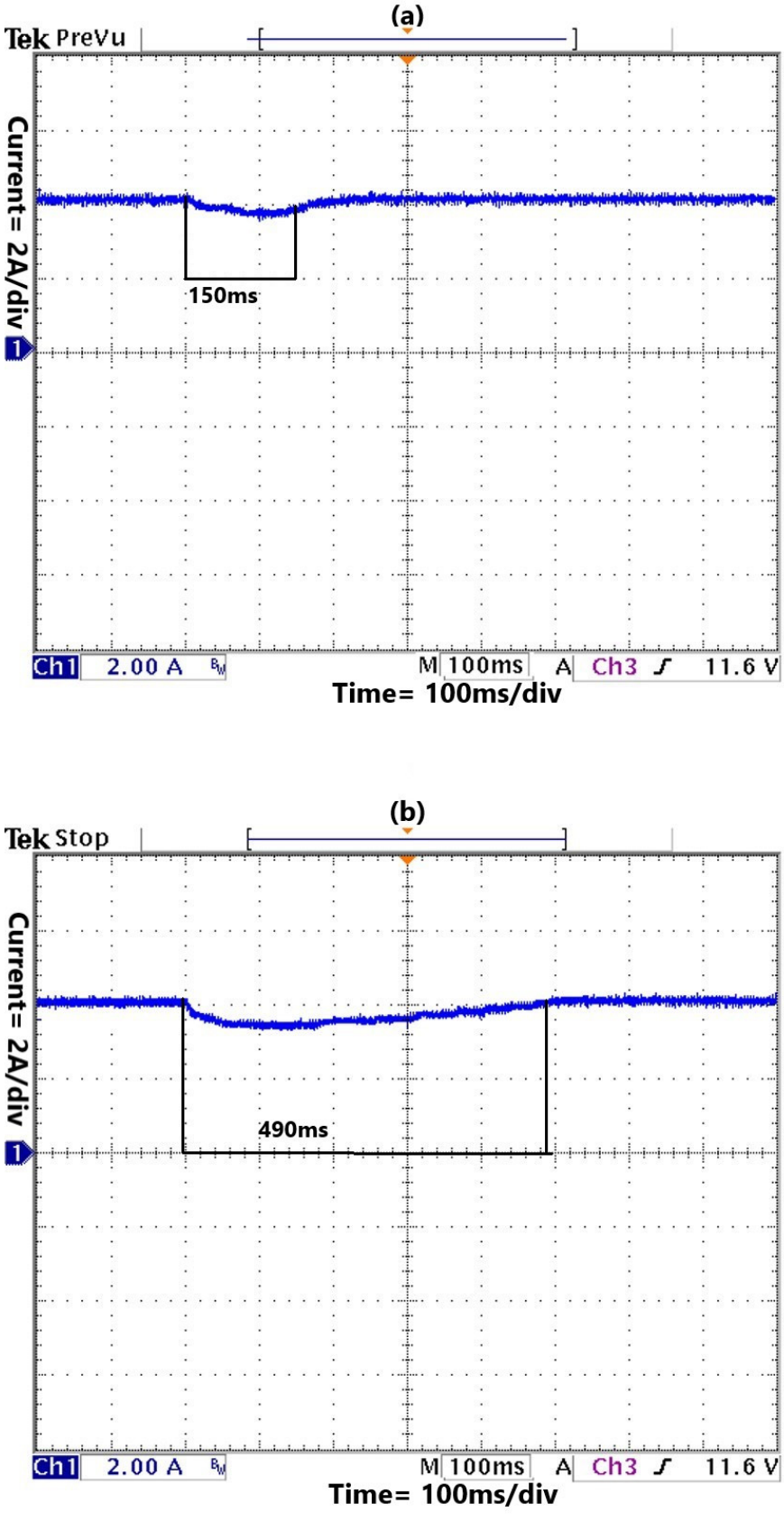


**Figure 19.** *Cont*.

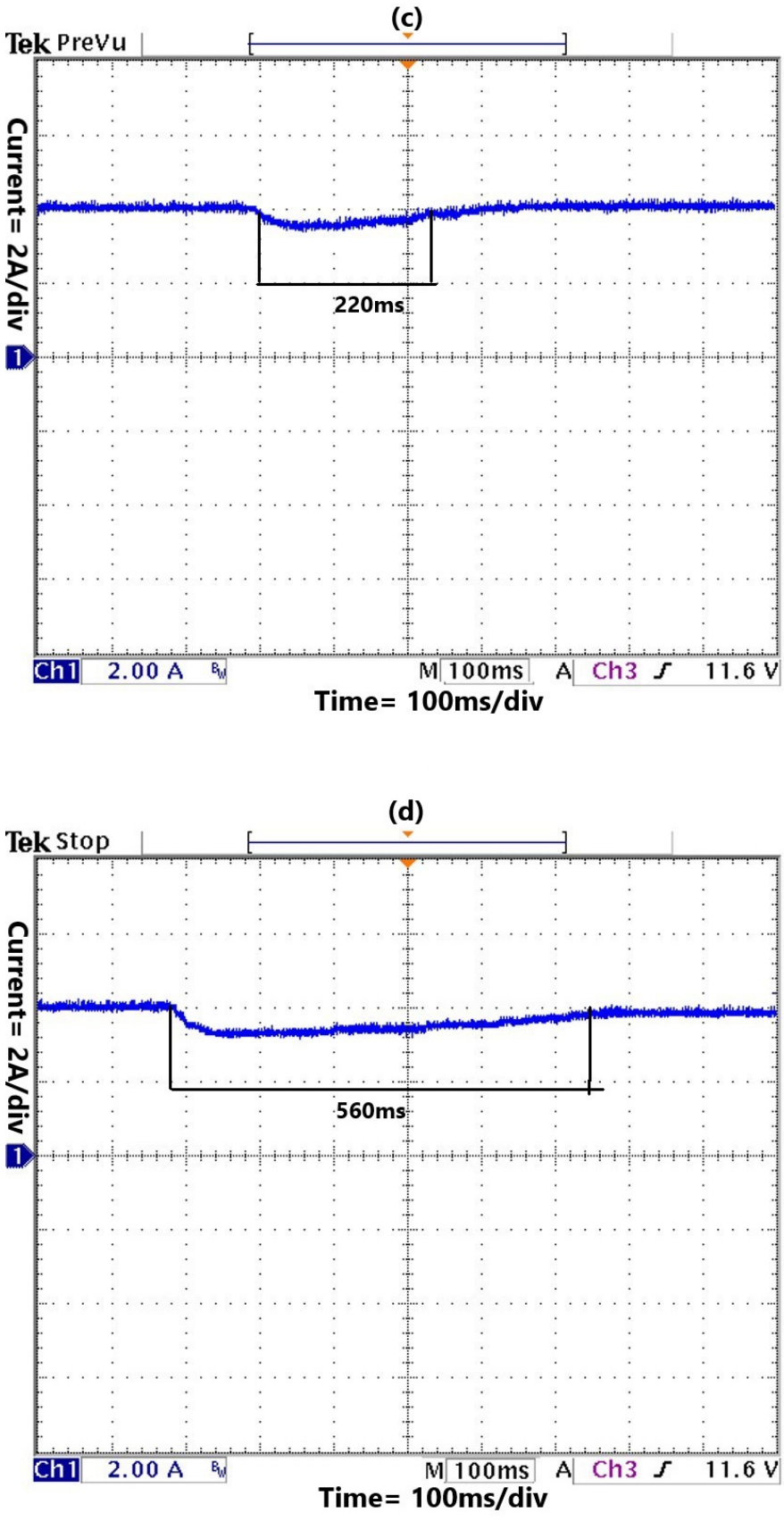


**Figure 19.** Experimental results when there is a 25% change in load resistance: (**a**) FCC; (**b**) LCFF; (**c**) MBPS; (**d**) PI.

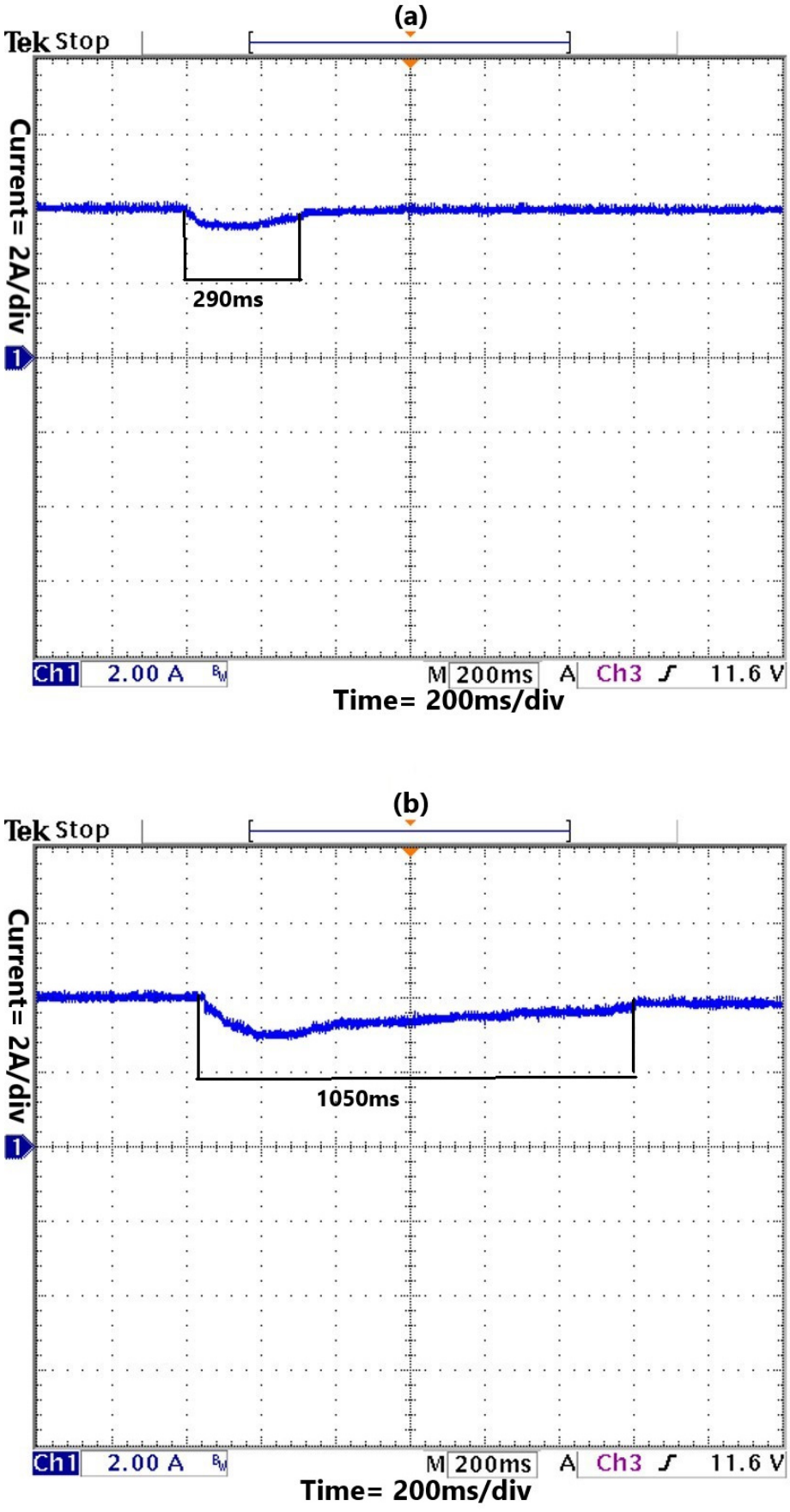


**Figure 20.** *Cont*.

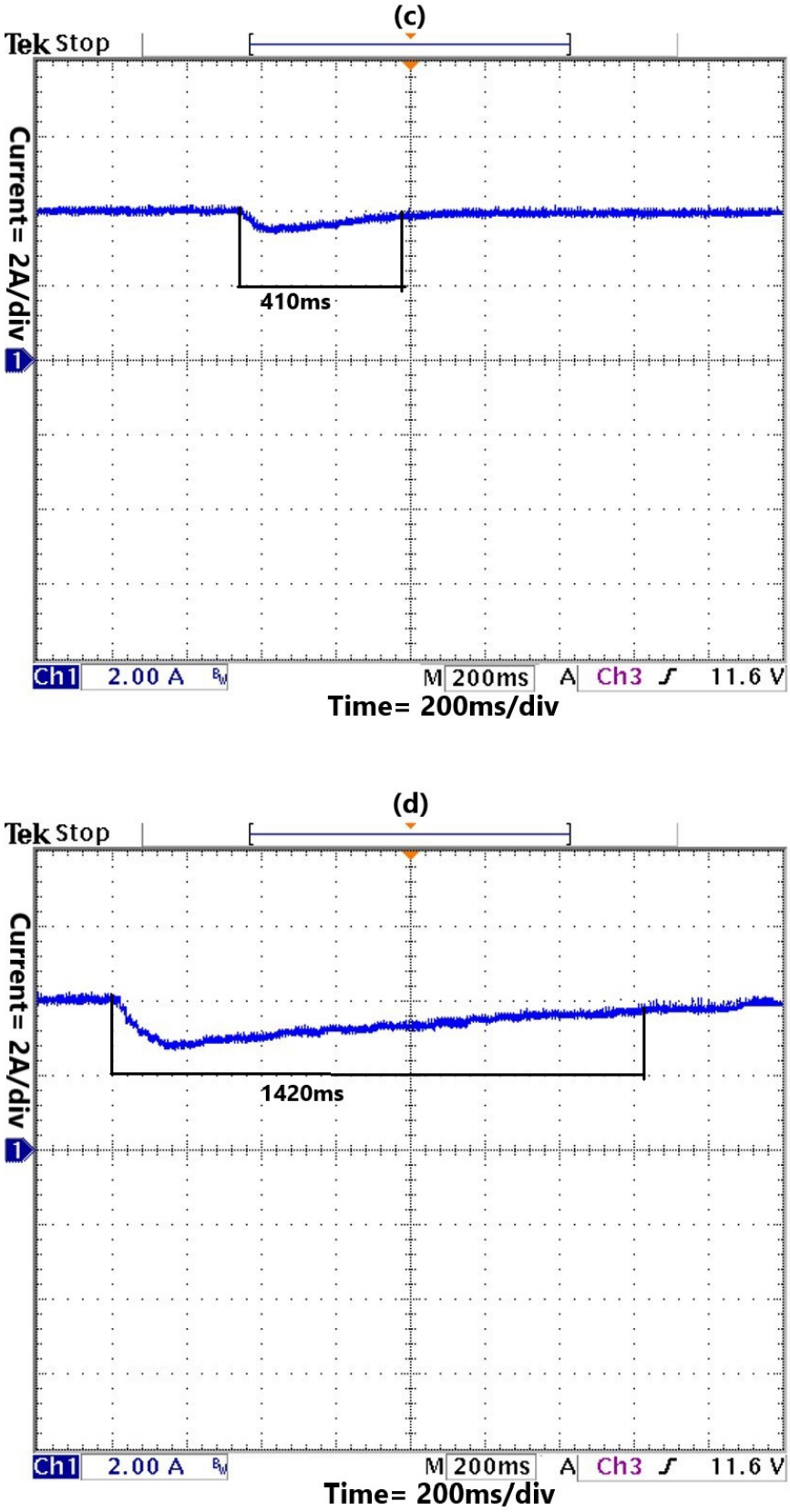


**Figure 20.** Experimental results when there is a 50% change in load resistance: (**a**) FCC; (**b**) LCFF; (**c**) MBPS; (**d**) PI.

**Table 4.** Summary of experimental results.

| Test Cases | FCC | | LCFF | | MBPS | | PI | |
|---|---|---|---|---|---|---|---|---|
| | **Δt** | **Δi** | **Δt** | **Δi** | **Δt** | **Δi** | **Δt** | **Δi** |
| 4 A (ref) | 30 ms | -/- | 160 ms | -/- | 55 ms | -/- | 280 ms | -/- |
| 25% Load change | 150 ms | 0.3 A | 490 ms | 0.55 A | 220 ms | 0.4 A | 560 ms | 0.75 A |
| 50% Load change | 290 ms | 0.4 A | 1050 ms | 1 A | 410 ms | 0.6 A | 1420 ms | 1.2 A |
| Input voltage change (75 V to 65 V) | Neg. | -/- | 170 ms | 0.3 A | Neg. | -/- | 210 ms | 0.35 A |
| Input voltage change (65 V to 75 V) | Neg. | -/- | 240 ms | 0.2 A | Neg. | -/- | 290 ms | 0.2 A |

**Table 5.** Comparison of controllers in terms of robustness and effectiveness under various disturbances.

| Control Strategy | Start Up | Change in Reference Current | Change in Load | Change in Input Voltage |
|---|---|---|---|---|
| FCC | Fastest | Faster | Fastest | Fastest |
| LCFF | Slow | Slow | Slower | Fast |
| MBPS | Faster | Fast | Faster | Fastest |
| PI | Slower | Slower | Slow | Slow |

## 6. Conclusions

Due to the high power density, inherent zero-voltage-switching (ZVS), and high voltage-conversation ratio, the current-source-based isolated dual-active-bridge DAB–DC/DC converters are extensively used for charging EVs under constant-current mode. A vital prerequisite for a high-performance current-source-based DAB–DC/DC converter is to attain the reference output current swiftly and correctly under severe operating conditions such as a change in the load and input voltage, during startup, and during a change in the desired output current. Therefore, to attain the fast dynamic characteristics, based on the direct-power control strategy and energy conversation concept, a fast current controller for a single-phase-shift dual-active-bridge DC/DC converter as a controlled-current source is proposed and analyzed in this paper. To verify the effectiveness and dynamic performance of the proposed controller, a constant-current-based DAB–DC/DC converter is modeled and simulated in MATLAB/Simulink software and a scaled-down 300 W lab prototype DAB–DC/DC converter is designed with the TMS320F28335 DSP controller of Texas Instruments. Both the experimental and simulation results have validated the effectiveness of the proposed control strategy. The proposed control scheme has very good robustness, as it is not dependent on circuit parameters, i.e., inductor value, switching frequency, and transformer turns ratio. The salient features of the proposed current control strategy are as follows:

1. During variations in the load and input voltage, compared with the MBPS, LCFF, and PI current controller, the proposed current controller has the best dynamic response and tracks the desired output current in the shortest time, with negligible current overshoot/undershoot.
2. Moreover, during the startup process or change in reference output current conditions, compared with the other three controllers, the proposed FCC strategy can significantly attain the fastest dynamic response.

With the rapid evolution of technology in power electronics, the application of DC/DC converters is not just limited to EV charging. DC/DC converters are extensively used in DC microgrids, photovoltaic systems, railway traction systems, energy-storage systems, solid-state transformers, etc. All these mentioned applications require robust dynamic response against disturbances. Thus, our proposed control can be useful in these applications as well. Furthermore, in this study, the proposed current controller is implemented with the present SPS modulation, which is suitable for the abovementioned applications. Simplicity and ease of implementation is the main advantage of this switching technique. Though it has achieved a fast dynamic response, it can suffer from high-current stress under light-load conditions due to negative power flow in SPS modulation, which is the limitation of this research. However, to minimize this current stress and enhance the ZVS range, the proposed current-control scheme can further be considered and implemented in the

future with other switching modulation techniques such as extended-phase-shift (EPS), dual-phase-shift (DPS), and triple-phase-shift (TPS).

**Author Contributions:** M.H.A., M.M.H. and M.A.C.: conceptualization, methodology, software, and writing—original draft; M.H.A., M.T., Z.A.M., J.S., N.A.R. and M.M.H.: writing—review and editing; Z.A.M., M.T. and N.A.R.: data curation; M.M.H., M.H.A. and N.A.R.: writing—review and editing. All authors have read and agreed to the published version of the manuscript.

**Funding:** This research received no external funding.

**Data Availability Statement:** Not applicable.

**Conflicts of Interest:** The authors declare no conflict of interest.

## References

1. Shen, M.; Huang, W.; Chen, M.; Song, B.; Zeng, G.; Zhang, Y. (Micro) Plastic Crisis: Un-Ignorable Contribution to Global Greenhouse Gas Emissions and Climate Change. *J. Clean. Prod.* **2020**, *254*, 120138. [CrossRef]
2. Dai, Q.; Kelly, J.C.; Gaines, L.; Wang, M. Life Cycle Analysis of Lithium-Ion Batteries for Automotive Applications. *Batteries* **2019**, *5*, 48. [CrossRef]
3. Ashfaq, M.; Butt, O.; Selvaraj, J.; Rahim, N. Assessment of Electric Vehicle Charging Infrastructure and Its Impact on the Electric Grid: A Review. *Int. J. Green Energy* **2021**, *18*, 657–686. [CrossRef]
4. Skrúcaný, T.; Kendra, M.; Stopka, O.; Milojević, S.; Figlus, T.; Csiszár, C. Impact of the electric mobility implementation on the greenhouse gases production in central European countries. *Sustainability* **2019**, *11*, 4948. [CrossRef]
5. Kopelias, P.; Demiridi, E.; Vogiatzis, K.; Skabardonis, A.; Zafiropoulou, V. Connected & autonomous vehicles–Environmental impacts–A review. *Sci. Total Environ.* **2020**, *712*, 135237. [PubMed]
6. IEA. *Global EV Outlook*; IEA: Paris, France, 2019.
7. Butt, O.M.; Butt, T.M.; Ashfaq, M.H.; Talha, M.; Raihan, S.R.S.; Hussain, M.M. Simulative Study to Reduce DC-Link Capacitor of Drive Train for Electric Vehicles. *Energies* **2022**, *15*, 4499. [CrossRef]
8. Bharathidasan, M.; Indragandhi, V. Review of Power Factor Correction (PFC) AC/DC-DC Power Electronic Converters for Electric Vehicle Applications. *IOP Conf. Ser. Mater. Sci. Eng.* **2020**, *906*, 012006. [CrossRef]
9. Hussain, M.M.; Akram, R.; Memon, Z.A.; Nazir, M.H.; Javed, W.; Siddique, M. Demand Side Management Techniques for Home Energy Management Systems for Smart Cities. *Sustainability* **2021**, *13*, 11740. [CrossRef]
10. Kheraluwala, M.; Gascoigne, R.W.; Divan, D.M.; Baumann, E.D. Performance characterization of a high-power dual active bridge DC-to-DC converter. *IEEE Trans. Ind. Appl.* **1992**, *28*, 1294–1301. [CrossRef]
11. Zhao, B.; Song, Q.; Liu, W.; Sun, Y. Overview of dual-active-bridge isolated bidirectional DC–DC converter for high-frequency-link power-conversion system. *IEEE Trans. Power Electron.* **2015**, *29*, 4091–4106. [CrossRef]
12. Zhao, B.; Song, Q.; Liu, W. Experimental comparison of isolated bidirectional DC–DC converters based on all-Si and all-SiC power devices for next-generation power conversion application. *IEEE Trans. Ind. Electron.* **2016**, *61*, 1389–1393. [CrossRef]
13. Huisman, T. A Dual Active Bridge DC-DC Converter for Automotive Applications: Design of a High Efficiency Bidirectional DAB Converter for the Lightyear One. Master's Thesis, Delft University of Technology, Delft, The Netherland, 2020.
14. Shi, R.; Semsar, S.; Lehn, P.W. Constant current fast charging of electric vehicles via a DC grid using a dual-inverter drive. *IEEE Trans. Ind. Electron.* **2017**, *64*, 6940–6949. [CrossRef]
15. Fei, L.; Shahzad, M.; Abbas, F.; Muqeet, H.A.; Hussain, M.M.; Bin, L. Optimal Energy Management System of IoT-Enabled Large Building Considering Electric Vehicle Scheduling, Distributed Resources, and Demand Response Schemes. *Sensors* **2022**, *22*, 7448. [CrossRef] [PubMed]
16. Cardozo, D.D.M.; Balda, J.C.; Trowler, D.; Mantooth, H.A. Novel nonlinear control of Dual Active Bridge using simplified converter model. In Proceedings of the 2010 Twenty-Fifth Annual IEEE Applied Power Electronics Conference and Exposition (APEC), Palm Springs, CA, USA, 21–25 February 2010; pp. 321–327.
17. Kanaan, H.Y.; Caron, M.; Al-Haddad, K. Design and implementation of a two-stage grid-connected high efficiency power load emulator. *IEEE Trans. Power Electron.* **2013**, *29*, 3997–4006. [CrossRef]
18. Alvarez-Ramirez, J.; Cervantes, I.; Espinosa-Perez, G.; Maya, P.; Morales, A. A stable design of PI control for DC-DC converters with an RHS zero. *IEEE Trans. Circuits Syst. I Fundam. Theory Appl.* **2001**, *48*, 103–106. [CrossRef]
19. Segaran, D.; McGrath, B.; Holmes, D. Adaptive dynamic control of a bi-directional DC-DC converter. In Proceedings of the 2013 IEEE Energy Conversion Congress and Exposition, Denver, CO, USA, 15–19 September 2013; pp. 1442–1449.
20. Segaran, D.; Holmes, D.G.; McGrath, B.P. Enhanced load step response for a bidirectional DC–DC converter. *IEEE Trans. Power Electron.* **2016**, *28*, 371–379. [CrossRef]
21. Xu, G.; Sha, D.; Zhang, J.; Liao, X. Unified boundary trapezoidal modulation control utilizing fixed duty cycle compensation and magnetizing current design for dual active bridge DC–DC converter. *IEEE Trans. Power Electron.* **2016**, *32*, 2243–2252. [CrossRef]
22. Bai, H.; Nie, Z.; Mi, C.C. Experimental comparison of traditional phase-shift, dual-phase-shift, and model-based control of isolated bidirectional DC–DC converters. *IEEE Trans. Power Electron.* **2016**, *25*, 1444–1449. [CrossRef]

23. Riaz, M.; Sałabun, W.; Athar Farid, H.M.; Ali, N.; Wątróbski, J. A robust q-rung orthopair fuzzy information aggregation using Einstein operations with application to sustainable energy planning decision management. *Energies* **2020**, *13*, 2155. [CrossRef]
24. Riaz, M.; Athar Farid, H.M.; Shakeel, H.M.; Arif, D. Cost Effective Indoor HVAC Energy Efficiency Monitoring based on Intelligent Decision Support System under Fermatean Fuzzy Framework. *Sci. Iran.* **2022**. [CrossRef]
25. Qin, D.; Sun, Q.; Ma, D.; Sun, J. Model Predictive control of dual-active-bridge based fast battery charger for plug-in hybrid electric vehicle in the future grid. In Proceedings of the 2019 IEEE Innovative Smart Grid Technologies-Asia (ISGT Asia), Chengdu, China, 21–24 May 2019; pp. 2162–2166.
26. Gao, G.; Lei, W.; Cui, Y.; Li, K.; Hu, X.; Xu, J.; Lv, G. Model Predictive Control of Dual Active Bridge Converter Based on the Lookup Table Method. In Proceedings of the 2019 IEEE 10th International Symposium on Power Electronics for Distributed Generation Systems (PEDG), Xi'an, China, 3–6 June 2019; pp. 183–186.
27. Jeung, Y.-C.; Lee, D.-C. Voltage and current regulations of bidirectional isolated dual-active-bridge DC–DC converters based on a double-integral sliding mode control. *IEEE Trans. Power Electron.* **2018**, *34*, 6937–6946. [CrossRef]
28. Li, K.; Yang, Y.; Tan, S.-C.; Hui, R.S.-Y. Sliding-mode-based direct power control of dual-active-bridge DC-DC converters. In Proceedings of the 2019 IEEE Applied Power Electronics Conference and Exposition (APEC), Anaheim, CA, USA, 17–21 March 2019; pp. 188–192.
29. Lee, S.; Jeung, Y.-C.; Lee, D.-C. Voltage balancing control of IPOS modular dual active bridge DC/DC converters based on hierarchical sliding mode control. *IEEE Access* **2019**, *7*, 9989–9997. [CrossRef]
30. Farooq, Z.; Zaman, T.; Khan, M.A.; Muyeen, S.; Ibeas, A. Artificial neural network based adaptive control of single phase dual active bridge with finite time disturbance compensation. *IEEE Access* **2019**, *7*, 112229–112239. [CrossRef]
31. Liu, B.; Zha, Y.; Zhang, T.; Chen, S. Fuzzy logic control of dual active bridge in solid state transformer applications. In Proceedings of the 2016 Tsinghua University-IET Electrical Engineering Academic Forum, Beijing, China, 13–15 May 2016; pp. 1–4.
32. Alonso, A.R.R.; Sebastian, J.; Lamar, D.G.; Hernando, M.M.; Vazquez, A. An overall study of a Dual Active Bridge for bidirectional DC/DC conversion. In Proceedings of the 2010 IEEE Energy Conversion Congress and Exposition, Atlanta, Georgia, USA, 12–16 September 2010; pp. 1129–1135.
33. Shah, S.S.; Bhattacharya, S. A simple unified model for generic operation of dual active bridge converter. *IEEE Trans. Ind. Electron.* **2018**, *66*, 3486–3495. [CrossRef]
34. Takagi, K.; Fujita, H. Dynamic control and performance of a dual-active-bridge DC–DC converter. *IEEE Trans. Power Electron.* **2017**, *33*, 7858–7866. [CrossRef]
35. Gui, Y.; Kim, C.; Chung, C.C.; Guerrero, J.M.; Guan, Y.; Vasquez, J.C. Improved direct power control for grid-connected voltage source converters. *IEEE Trans. Ind. Electron.* **2018**, *65*, 8041–8051. [CrossRef]
36. Wai, R.-J.; Yang, Y. Design of backstepping direct power control for three-phase PWM rectifier. *IEEE Trans. Ind. Appl.* **2019**, *55*, 3160–3173. [CrossRef]
37. Benbouhenni, H. Direct power control of a DFIG fed by a seven-level inverter using SVM strategy. *Int. J. Smart Grid* **2019**, *3*, 54–62.
38. Youssef, E.; Costa, P.B.; Pinto, S.F.; Amin, A.; El Samahy, A.A. Direct power control of a single stage current source inverter grid-tied PV system. *Energies* **2020**, *13*, 3165. [CrossRef]
39. Song, W.; Hou, N.; Wu, M. Virtual direct power control scheme of dual active bridge DC–DC converters for fast dynamic response. *IEEE Trans. Power Electron.* **2017**, *33*, 1750–1759. [CrossRef]
40. Tiwary, N.; Venkataramana, N.N.; Panda, A.k.; Narendra, A. Direct Power Control of Dual Active Bridge Bidirectional DC-DC Converter. In Proceedings of the 2019 International Conference on Power Electronics, Control and Automation (ICPECA), New Delhi, India, 16–17 November 2019; pp. 1–4.
41. Ríos, S.J.; Pagano, D.J.; Lucas, K.E. Bidirectional Power Sharing for DC Microgrid Enabled by Dual Active Bridge DC-DC Converter. *Energies* **2021**, *14*, 404. [CrossRef]
42. Shao, S.; Chen, L.; Shan, Z.; Gao, F.; Chen, H.; Sha, D.; Dragicevic, T.G. Modeling and Advanced Control of Dual Active Bridge DC-DC Converters: A Review. *IEEE Trans. Power Electron.* **2021**, *37*, 1524–1547. [CrossRef]
43. Herrera-Jaramillo, D.A.; Gonzalez Montoya, D.; Henao-Bravo, E.E.; Ramos-Paja, C.A.; Saavedra-Montes, A.J. Systematic analysis of control techniques for the dual active bridge converter in photovoltaic applications. *Int. J. Circuit Theory Appl.* **2021**, *49*, 3031–3052. [CrossRef]
44. Sanders, S.R.; Noworolski, J.M.; Liu, X.Z.; Verghese, G.C. Generalized averaging method for power conversion circuits. *IEEE Trans. Power Electron.* **1991**, *6*, 251–259. [CrossRef]
45. Erni, I.R.; Vidal-Idiarte, E.; Calvente, J.; Guasch-Pesquer, L. Small signal modelling for variable frequency control with maximum efficiency point tracking of DAB converter. *IEEE Access* **2021**, *9*, 85289–85299. [CrossRef]
46. Rolak, M.; Twardy, M.; Soból, C. Generalized Average Modeling of a Dual Active Bridge DC-DC Converter with Triple-Phase-Shift Modulation. *Energies* **2022**, *15*, 6092. [CrossRef]
47. Tolstov, G.P. *Fourier Series*; Courier Corporation: Chelmsford, MA, USA, 2012.
48. Huang, J.; Li, Z.; Shi, L.; Wang, Y.; Zhu, J. Optimized modulation and dynamic control of a three-phase dual active bridge converter with variable duty cycles. *IEEE Trans. Power Electron.* **2018**, *34*, 2856–2873. [CrossRef]